Master's thesis

NTNU
Norwegian University of Science and Technology
Faculty of Information Technology and Electrical Engineering
Department of Electronic Systems

Selma Tofte Thiis

Simulation and Characterization of Mesoporous Optical Rib Waveguides for use in Near Infrared Liquid Sensing

Master's thesis in Electronic Systems Design and Innovation
Supervisor: Astrid Aksnes
Co-supervisor: Jana Jágerská, Sebastián Alberti
July 2023

NTNU
Norwegian University of
Science and Technology

Selma Tofte Thiis

Simulation and Characterization of Mesoporous Optical Rib Waveguides for use in Near Infrared Liquid Sensing

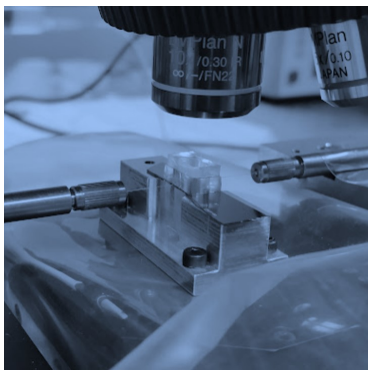

Master's thesis in Electronic Systems Design and Innovation
Supervisor: Astrid Aksnes
Co-supervisor: Jana Jágerská, Sebastián Alberti
July 2023

Norwegian University of Science and Technology
Faculty of Information Technology and Electrical Engineering
Department of Electronic Systems

NTNU
Norwegian University of
Science and Technology

Problem Description

On-chip devices such as integrated optical waveguides, are ever emerging as efficient and non invasive near infrared (NIR) sensors. The light-matter interaction of analytes in the top cladding of the waveguide give premise for sensitive analyte detection. To further enhance light-analyte interaction in gas sensing, a design of using a mesoporous waveguide core has been investigated at the Arctic University of Norway (UiT) (Alberti et al.; unpublished). Their work has demonstrated that gas diffusing into pores interacts with the electromagnetic field in a way that substantially increases the light-matter interaction of the analyte in comparison to a similar waveguide with a solid core.

To further advance this work, this thesis aims to investigate and experiment with the possibility of using a mesoporous optical waveguide design in liquid sensing. Simulations using Ansys Lumerical's MODE Solver will be performed to study the relation between confinement factor in a liquid cladding and the waveguide's porosity. Also, the confinement factor in different solvents such as water, ethanol and methanol on the mesoporous waveguide, will be simulated and studied.

A microfluidic cell to retain solvents onto the waveguide as the top cladding, will be fabricated to fit a mesoporous optical waveguide chip fabricated by Sebastián Alberti in December 2023 using the Sol-gel method. The microfluidic cell will be customized using Polydimethylsiloxane (PDMS) fabrication and joined to the mesoporous waveguide chip in the NTNU NanoLab cleanroom.

Characterizations of the mesoporous optical waveguide will be performed using ellipsometry and transmission measurements in a tunable NIR laser setup. The aim of the latter is to explore the transmission in the mesoporous optical waveguide when exposed to the different solutions water, ethanol and methanol and analyse the possibilities for liquid sensing using this waveguide design.

Abstract

The increasing demand for efficient and sensitive biomedical sensing applications has advanced the development of lab-on-a-chip (LOC) photonic devices. Thus, optical waveguides, traditionally used for transmission purposes, are increasingly recognized for their potential in sensing applications. This thesis explores the utilization of a mesoporous optical waveguide design for liquid sensing. The main objectives are to examine the correlation between porosity and confinement factor in mesoporous optical waveguides, analyse the confinement in mesoporous optical waveguides with liquid solutions as top cladding, and explore the effect on transmission when using liquid as top cladding.

Simulations using Ansys Lumerical's MODE Solver were performed to study the correlation between the confinement factor in a liquid cladding and the waveguide's porosity. Additionally, a microfluidic cell was fabricated using Polydimethylsiloxane (PDMS) to retain solvents onto the waveguide as the top cladding. The mesoporous optical waveguide chip, fabricated using the Sol-gel method, was customized and joined to the microfluidic cell in the NTNU NanoLab cleanroom. Characterization of the waveguide was carried out using ellipsometry and transmission measurements with a tunable NIR laser setup.

The results demonstrated that the mesoporous optical waveguide design exhibited enhanced light-matter interaction with liquid analytes in the top cladding, compared to using air as top cladding. Furthermore, the simulations revealed that when using liquids, increased porosity in the core gave a higher confinement factor, indicating that the design is preferable for liquid sensing applications with highly porous cores. The transmission measurements confirmed the simulated changes in transmission spectra due to the different solutions used as top cladding. Of the solutions tested, the one with the lowest absorption in the experimental range, ethanol, experienced the highest transmission, as expected from theory and simulations.

The findings of this research provide a solid foundation for future investigations into the use of mesoporous optical waveguides for liquid sensing, particularly in biomedical applications. The results demonstrate the potential of this waveguide design to enhance sensitivity and detection capabilities in the field of biomedical sensing. Suggestions for further research and improvements to the experimental setup are also discussed.

Sammendrag

Den økende etterspørselen etter effektive biomedisinske sensorer har ført til utvikling av lab-on-a-chip (LOC) fotoniske måleenheter. Dermed har optiske bølgeledere, tradisjonelt brukt til signaloverføring, i økende grad blitt anerkjent for deres potensiale som målesensorer. Denne masteroppgaven utforsker bruken av et mesoporøst optisk bølgelederdesign for væskesensing. Hovedmålene er å undersøke sammenhengen mellom porøsitet og inneslutningsfaktor i mesoporøse optiske bølgeledere, samt å analysere feltets inneslutning i mesoporøse optiske bølgeledere med væskeløsninger som toppkappe. I tillegg, er et mål å utforske effekten på transmisjon ved bruk av væske som toppkappe.

Simuleringer ved bruk av Ansys Lumericals MODE Solver ble utført for å studere korrelasjonen mellom inneslutningsfaktoren i en væskekappe og bølgelederens porøsitet. I tillegg ble en mikrofluidisk celle fremstilt ved bruk av polydimetylsiloksan (PDMS) for å introdusere løsemidler på bølgelederen som toppkappe. Den mesoporøse optiske bølgelederbrikken, fremstilt ved bruk av Sol-gel-metoden, ble tilpasset og koblet til den mikrofluidiske cellen i NTNU NanoLabs renrom. Karakterisering av bølgelederen ble utført ved bruk av ellipsometri og transmisjonsmålinger med et justerbart NIR-laseroppsett.

Resultatene viste at det mesoporøse optiske bølgelederdesignet innehar forbedret lys-materie-interaksjon med flytende analytter i toppkappen, sammenlignet med bruk av luft som toppkappe. Videre avslørte simuleringene at ved bruk av væsker gir økt porøsitet i kjernen en høyere inneslutningsfaktor, noe som indikerer at et design med svært porøse kjerner er å foretrekke for væskesensorapplikasjoner. Transmisjonsmålingene bekreftet de simulerte endringene i transmisjonsspektrene på grunn av de forskjellige løsningene som ble brukt som toppkappe. Av løsningene som ble testet, opplevde den med lavest absorpsjon i forsøksområdet, etanol, høyest transmisjon, som forventet fra teori og simuleringer.

Funnene i denne oppgaven gir et solid grunnlag for fremtidige undersøkelser for bruken av mesoporøse optiske bølgeledere i væskesensing, spesielt i biomedisinske applikasjoner. Resultatene viser potensialet dette bølgelederdesignet har for å forbedre følsomhet og deteksjonsevne innen biomedisinsk sensing. Forslag til videre forskning og forbedringer av forsøksoppsettet diskuteres også.

Preface

This thesis is the final piece of work submitted as a part of my degree of Masters of Science in Electronic Systems Design and Innovation with a specialization in Nano Electronics and Photonics at the Norwegian University of Science and Technology (NTNU). The thesis completes five years of study, research and exploration into the field of electronic systems, nanotechnology and photonics. The years have been filled with numerous challenges, discoveries and growth and it is with great sense of accomplishment I present this culmination of my last year of study.

The thesis is a continuation of my work on a specialization project presented in January of 2023, with focus on simulations for optimization of porous optical waveguides to use in gas sensing and characterization of porous optical waveguides using ellipsometry. Some parts of the report on the specialization project are in part reproduced and expanded on in this thesis, more specifically parts of the theoretical background in Chapter 2 and selected methods and procedures in Chapter 3 and 4. As this report aims to study the use of mesoporous optical waveguides for liquid sensing, these sections are elaborated to reflect this.

Acknowledgements

This thesis would not have been possible without support and encouragement. Firstly, I want to thank my supervisor Astrid Aksnes for good advice, immense support and motivation, also in times of low morale. Also, I thank my co-supervisors Jana Jágerská for her invaluable guidance and feedback, and Sebastián Alberti for support and help in fabrication and ellipsometry measurements.

Furthermore, I want to thank Jens Høvik and other members of the photonics group at NTNU for assistance and instruction in the photonics lab, as well as engineers at NTNU Nanolab for offering training and advice in the cleanroom.

Finally, I extend a thank you to my father Thomas Thiis for additional help in the structuring and proof-reading of my thesis, my mother Hege Hauge Tofte for emotional support and my sisters for reminding me that I am in fact older than them. Lastly, thank you to my fellow students for making mediocre coffee, but being great companionship for five years.

Selma Tofte Thiis, 2^{nd} *July* 2023

Contents

List of Abbreviations

a.u.	Arbitrary Units
EM	Electromagnetic
FDE	Finite Difference Eigenmode
IR	Infrared
LOC	Lab-on-a-chip
NA	Numerical Aperture
NIR	Near Infrared
NMBU	Norwegian University of Life Sciences
NTNU	Norwegian University of Science and Technology
PDMS	Polydimethylsiloxane
PML	Perfectly Matched Layer
Si	Silicon
SiO_2	Silicon Dioxide
TE	Transverse Electric
TEM	Transverse Electromagnetic
TiO_2	Titanium Dioxide
TM	Transverse Magnetic
UiT	The Arctic University of Norway

Chapter 1

Introduction

1.1 Motivation

Research into ways to improve and streamline detection of disease in medicine has long been an important focus in science. Efficient and sensitive biomedical sensors in a lab-on-a-chip (LOC) configuration for analyte detection, have recently seen fast development due to their portability, reduced cost and fast sensing ability.

While often used for transmission purposes, optical waveguides are increasingly recognised for their potential in sensing applications. Optical waveguide sensing is an ever emerging technology with research including evanescent field confinement sensing in [1] and optical slot-waveguide based biochemical sensors in [2]. The sensitivity of optical waveguides allows for both gas and liquid sensing when using functionalization of the waveguide surface and preconcentration of analytes in either gases or liquid solutions. The waveguide design involves a core surrounded by cladding, and the waveguide's guiding properties can easily be tuned by using materials with different refractive indices and different geometry. Sensing is possible by studying field interactions in the core and cladding of the waveguide. For instance, the molecular characteristics of an unknown cladding such as a preconcentrated solution with an analyte, may be revealed when the evanescent field propagation in the cladding affects the transmission in the waveguide.

Mesoporous optical waveguides have recently emerged as a more sensitive alternative to non-porous optical waveguides in gas sensing, with the use of a mesoporous dielectric core. The design has been investigated at at the Arctic University of Norway (UiT) (Alberti et al.; unpublished) and research has demonstrated how gas diffusion into pores significantly enhances the interaction between the electromagnetic field and the analyte, allowing for more sensitive detection. Building upon this research, this thesis aims to investigate and experiment with the utilization of a mesoporous optical waveguide design for liquid sensing applications, such as for biomedical analyte detection.

1.2 Objectives and Limitations

The main objectives of this thesis can be summarized to:

- Examine the correlation between porosity and confinement factor in mesoporous optical waveguides
- Analyse the confinement in mesoporous optical waveguides with liquid solutions as top cladding
- Explore the effect on transmission when using liquid as top cladding in mesoporous optical waveguides

The research involves simulations, fabrication and characterization of a mesoporous optical waveguide. Simulations are performed using Ansys Lumerical's MODE Solver to examine the correlation between the confinement factor in a liquid cladding, and the porosity of the waveguide. In addition, simulations of the transmission in the waveguide according to confinement factor when using different solutions are completed, to observe the expected results from transmission measurements and compare. Fabrication of a microfluidic cell to aid in solution containment on a mesoporous optical waveguide chip is carried out using Polydimethylsiloxane (PDMS). The microfluidic cell is fabricated, customized and joined to the mesoporous waveguide chip in the NTNU NanoLab cleanroom, and the waveguide chip used was fabricated by Sebastián Alberti in December 2023 using the Sol-gel method. Finally, characterization of the mesoporous optical waveguide is performed using ellipsometry and transmission measurements in a tunable NIR laser setup. The ellipsometry measurements were performed using the Semilab SE-2000 Spectroscopic Ellipsometer and the transmission measurements were conducted using the Thorlabs TLK-L1550M Tunable Laser Kit mounted with a lensed fiber input. The aim of the transmission measurements is to investigate the transmission characteristics of the mesoporous optical waveguide when subjected to the various solutions water, ethanol, and methanol, to analyze the potential applications of this waveguide design in liquid sensing.

1.3 Structure

To give an outline of the necessary theoretical base for this thesis, Chapter 2 presents background theory of guided wave optics, dielectric waveguides and effective medium approaches to calculate porosity. Furthermore, Chapter 3 provides insight into the different simulation, fabrication and characterization methods applied in the experimental procedures outlined in Chapter 4. Chapter 5 conveys the obtained results from simulations, fabrication efforts and characterization experiments, as well as discussion on the observations. Finally, the thesis conclusion is presented in Chapter 6, including suggestions for future work and research into the use of mesoporous optical waveguides for liquid sensing. For completeness, parts of the background theory, the method and procedure chapters are improved from the specialization project report written on the same topics in January 2023.

Chapter 2

Theoretical Background

Saleh and Teich give a good background to guided wave optics and waveguide theory in their book Fundamentals of Photonics, Third Edition. Their explanations, with insight from other references, are repeated in brief in section 2.1 and 2.2. For clarity, the chapters cited from the book are divided into separate references; [3], [4], [5]. Important terms in this thesis are absorption, dispersion, effective and group refractive index, modes in dielectric waveguides, the single-mode condition, confinement factor, waveguide geometries, losses in waveguides and coupling into optical waveguides. Moreover, theoretical background of spectral analysis and effective medium approaches to calculate porosity is needed in understanding results from characterizations in this thesis. This is outlined in sections 2.3 and 2.4. The theoretical background chapter is in part improved from the specialization project written in January 2023.

2.1 Guided Wave Optics

Understanding guided wave optics is essential to understand the figures of merit of this thesis, and is therefore described from the most basic theory of electromagnetic optics.

2.1.1 Electromagnetic Optics

The theory of guided light starts with the definition of electromagnetic fields and their behaviour in a medium or free space. Saleh and Teich explain in [3] how electromagnetic fields and wave propagation in a medium can be described with Maxwell's differential equations as shown in equations 2.1 - 2.4, where the field amplitudes of the electric- and magnetic field are $\boldsymbol{E}(\boldsymbol{r},t) = \boldsymbol{E}_0(\boldsymbol{r})cos(\omega t + \phi(\boldsymbol{r}))$ and $\boldsymbol{H}(\boldsymbol{r},t) = \boldsymbol{H}_0(\boldsymbol{r})cos(\omega t + \phi(\boldsymbol{r}))$ respectively. $\boldsymbol{r}$ is displacement, ω is angular frequency, and $\phi(\boldsymbol{r})$ the phase.

$$\nabla \times \boldsymbol{H} = \frac{\partial \boldsymbol{D}}{\partial t}, \quad \text{(Faraday's law)} \tag{2.1}$$

$$\nabla \times \boldsymbol{E} = -\frac{\partial \boldsymbol{B}}{\partial t}, \quad \text{(Ampère's law)} \tag{2.2}$$

$$\nabla \cdot \boldsymbol{B} = 0, \quad \text{(Gauss' Law)} \tag{2.3}$$

$$\nabla \cdot \boldsymbol{D} = 0, \quad \text{(Coulomb's law)} \tag{2.4}$$

Furthermore, eq. 2.5 and eq. 2.6 describe the electric $\boldsymbol{D}$ and magnetic $\boldsymbol{B}$ flux density in relation to the electric $\boldsymbol{E}$ and magnetic $\boldsymbol{H}$ field respectively. Here $\boldsymbol{P}$ is the polarization density, $\boldsymbol{M}$ the

magnetisation density, ϵ_0 the electric permittivity and μ the magnetic permeability.

$$\boldsymbol{D} = \epsilon_0 \boldsymbol{E} + \boldsymbol{P} \tag{2.5}$$

$$\boldsymbol{B} = \mu_0(\boldsymbol{H} + \boldsymbol{M}) \tag{2.6}$$

When working with and describing electromagnetic fields in optical devices such as waveguides, a linear, non-dispersive, homogeneous and isotropic media are often assumed. Furthermore, the light is assumed monochromatic. With these assumptions, the electric and magnetic flux density become $\boldsymbol{D} = \epsilon \boldsymbol{E}$ and $\boldsymbol{B} = \mu \boldsymbol{H}$ respectively, and lead to the following changes in Maxwell's equations shown in eq. 2.7-2.10 for source free media.

$$\nabla \times \boldsymbol{H} = j\omega\epsilon \boldsymbol{E}, \quad \text{(Faraday's law)} \tag{2.7}$$

$$\nabla \times \boldsymbol{E} = -j\omega\epsilon \boldsymbol{H} \quad \text{(Ampère's law)} \tag{2.8}$$

$$\nabla \cdot \boldsymbol{H} = 0, \quad \text{(Gauss' Law)} \tag{2.9}$$

$$\nabla \cdot \boldsymbol{E} = 0, \quad \text{(Coulomb's law)} \tag{2.10}$$

Optical devices such as waveguides often have different modes of operation, meaning different field distributions and oscillations. The transverse electromagnetic (TEM) modes can be used to analyze and understand these different modes. Figure 2.1 shows a TEM wave travelling in z direction, where $\boldsymbol{E}$ is the electric field, $\boldsymbol{H}$ is the magnetic field, $\boldsymbol{k}$ the wave vector and $\boldsymbol{S}$ is the Poynting's vector. $\boldsymbol{E}$, $\boldsymbol{H}$ and $\boldsymbol{k}$ are orthogonal of each other and are further explained below the figure.

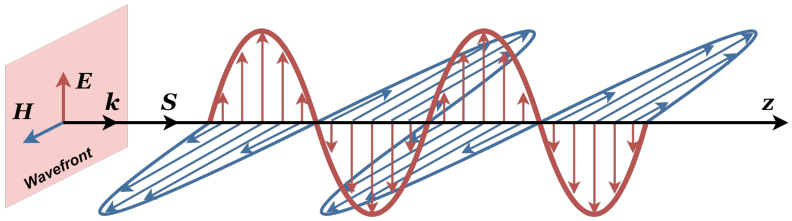

Figure 2.1: A TEM wave travelling in z direction.$\boldsymbol{E}$ is the electric field, $\boldsymbol{H}$ is the magnetic field, $\boldsymbol{k}$ the wave vector and $\boldsymbol{S}$ is the Poynting's vector. Adapted from [3].

For monochromatic electromagnetic TEM waves in a medium, the complex amplitude vectors for the electric- and magnetic field in equations 2.11 and 2.12 are relevant, where $\boldsymbol{k}$ is the wave vector with magnitude $\boldsymbol{k} = nk_0 = \omega\sqrt{\epsilon\mu}$ and n the refractive index [3].

$$\boldsymbol{H}(\boldsymbol{r}) = \boldsymbol{H}_0 e^{-j\boldsymbol{k}\cdot\boldsymbol{r}} \tag{2.11}$$

$$\boldsymbol{E}(\boldsymbol{r}) = \boldsymbol{E}_0 e^{-j\boldsymbol{k}\cdot\boldsymbol{r}} \tag{2.12}$$

Rearranging these using the Helmholtz equation, $\Delta^2 U + k^2 U = 0$, gives the harmonic functions in eq. 2.13 and eq. 2.14 that describe the harmonic movements related to the fields' angular frequency ω.

$$\boldsymbol{k} \times \boldsymbol{H}_0 = -\omega\epsilon \boldsymbol{E}_0 \tag{2.13}$$

$$\boldsymbol{k} \times \boldsymbol{E}_0 = \omega\mu \boldsymbol{H}_0 \tag{2.14}$$

These equations show that both $\boldsymbol{E}$ and $\boldsymbol{H}$ ought to be perpendicular to each other and to $\boldsymbol{k}$, giving a TEM wave [3]. Moreover, the complex Poynting vector in eq. 2.15 is used to represent the flow of electromagnetic power through a medium or free space and further assists to describe wave mode propagation.

$$\boldsymbol{S} = \frac{1}{2}\mathbf{E} \times \mathbf{H}^* \tag{2.15}$$

The magnitude of its real part, $|Re\{S\}|$, is the optical intensity, which is given by eq. 2.16, where $U(\boldsymbol{r})$ is the waves' amplitude.

$$I(\boldsymbol{r}) = |U(\boldsymbol{r})|^2 \tag{2.16}$$

The direction of the Poynting vector for a TEM wave is parallel to the wave vector $\boldsymbol{k}$ making the power flow normally to the wave fronts. The intensity of the wave is therefore given by eq. 2.17, assuming the electric and magnetic parts are equal.

$$I = c \cdot \frac{1}{2}\epsilon|\boldsymbol{E}_0|^2 \tag{2.17}$$

2.1.2 Absorption and Dispersion

For waves in a medium, absorption and dispersion play important roles in describing and understanding the propagation of the electromagnetic field as it interacts with the medium. α is the absorption coefficient of the medium and affects the intensity of the wave. β is the rate of change in the phase of the wave across z and is therefore called the propagation constant of the wave. The dispersion relation is the relation between β and the angular frequency ω. For a homogeneous medium, the dispersion relation is $\omega = c\beta$.

For monochromatic light, $\boldsymbol{k}$ can be expressed complex-valued as in eq. 2.18, where $k_0 = \omega/c_0$ is the wave number in free space [3].

$$k = k_0\sqrt{1 + \chi' + j\chi''} \tag{2.18}$$

Furthermore, expressing the wave vector as a combination of its real and imaginary parts gives an expression in terms of α and β shown in eq. 2.19.

$$k = \beta - j\frac{1}{2}\alpha \tag{2.19}$$

Moreover, the intensity of a wave propagating in a medium can also be expressed in terms of α and β. The complex amplitude $U(\boldsymbol{r})$ of the wave travelling in z direction, is given as in eq. 2.20, where B is the envelope of the wave.

$$U(\boldsymbol{r}) = Be^{-jkz} \tag{2.20}$$

By substituting the expression for the k in eq. 2.19, the amplitude U is expressed as in eq. 2.21.

$$U = Be^{-\frac{1}{2}\alpha z}e^{-j\beta z} \tag{2.21}$$

Inserting this amplitude into the equation for the intensity of a TEM wave in eq. 2.16, gives an equation for the intensity of a wave travelling in z-direction in terms of its propagation constant β and absorption coefficient α in eq. 2.22 [3], where I_0 is the incident intensity.

$$I = I_0e^{-\alpha z} \tag{2.22}$$

The Beer Lambert law [6] relates the intensity I and transmittance T of a wave to the absorbance A as shown in eq. 2.23.

$$A = -log_{10}\frac{I}{I_0} = -log_{10}T \tag{2.23}$$

Rearranging and incorporating 2.22, gives the relation between absorption coefficient α and transmittance T in eq. 2.24.

$$\alpha = -log_{10}(T)/x \tag{2.24}$$

2.1.3 Refractive Index, Effective Refractive Index and Group Index

The wave propagation in a medium also depends on the medium's refractive index. *Refractive index* is defined as the ratio between the speed of light in vacuum and in the medium as shown in equation eq. 2.25, where c is the speed of light in vacuum and v is the speed of light in the medium.

$$n = \frac{c}{v} \tag{2.25}$$

The refractive index n is affected by the wavelength of incident light, temperature, pressure, chemical composition and structure of the medium.

In addition to the refractive index, *effective refractive index* n_{eff} is used to further describe the wave propagation. Effective refractive index depends on the phase velocity of a guided wave propagating through a waveguide and is defined as the ratio of the speed of light in a vacuum to the phase velocity of the wave in the waveguide. The propagation constant β is the rate of change in phase, and effective refractive index can therefore be expressed as, shown in eq. 2.26 [3].

$$n_{eff} = \frac{\beta}{k_0} \tag{2.26}$$

The effective refractive index can also be expressed as in equation 2.27, where c is the speed of light in a vacuum, $v_p = \omega/k$ is the phase velocity of the wave in the waveguide, and f is the frequency of the guided wave [5].

$$n_{eff} = \frac{c}{v_p f} \tag{2.27}$$

n_{eff} is an indication on how a light wave is refracted, reflected and phase shifted as it travels through a waveguide and is therefore an important parameter in the design and analysis of waveguides. n_{eff} can be affected by the geometry and size of the waveguide.

While the effective refractive index is the rate of change in phase to the speed of light, *group refractive index* is the rate of change in phase to the frequency of the light. Group velocity and group refractive index are often used in analysis of wave propagation in optical devices such as optical fibers or waveguides. Group refractive index can be found from group velocity, which is the velocity of the envelope of the different amplitudes in a wave. Figure 2.2 shows the envelope wave in relation to the underlying wave [3].

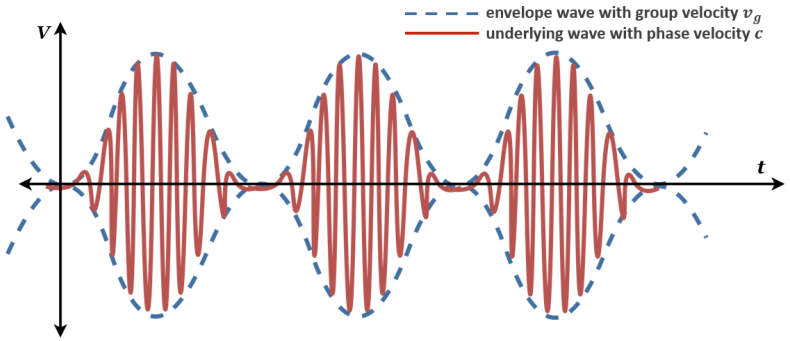

Figure 2.2: Illustration of envelope wave with group velocity v_g and underlying wave with phase velocity c of an electromagnetic field.

Group velocity is found by eq. 2.28 where ω is the angular frequency and $\beta = \frac{\omega n_{eff}(\omega)}{c_0}$ is the frequency dependent dispersion relation.

$$v_g = \frac{d\omega}{d\beta} \tag{2.28}$$

Furthermore, it can also be represented with the wavelength dependent refractive index $n(\lambda_0)$ by using eq. 2.29, eq. 2.30 and the chain rule.

$$\beta = \frac{\omega n(\lambda_0)}{c_0} = \frac{2\pi n(\lambda_0)}{\lambda_0} \tag{2.29}$$

$$\lambda_0 = \frac{2\pi c_0}{\omega} \tag{2.30}$$

This gives the group velocity v_g shown in eq. 2.31, and rearranging for n_g gives the group refractive index n_g.

$$v_g = \frac{c_0}{n_g} \quad \rightarrow \quad n_g = \frac{c_0}{v_g} \tag{2.31}$$

The group refractive index n_g can also be represented as in eq. 2.32.

$$n_g = n + \omega \frac{dn}{d\omega} \tag{2.32}$$

2.2 Dielectric Waveguides

Assuming a linear, non-dispersive, homogeneous and isotropic medium, electromagnetic waves can be guided using mirrored and dielectric waveguides. This thesis will focus on dielectric waveguides. Following is a theoretical explanation on light guiding in dielectric waveguides and ways to analyse propagation in waveguides. Additionally follows an outline of 3 different geometries for dielectric waveguides; two-dimensional rectangular, rib and strip waveguides.

2.2.1 Total Internal Reflection and Self-Consistency Condition

A basic planar dielectric slab waveguide is shown in figure 2.3.

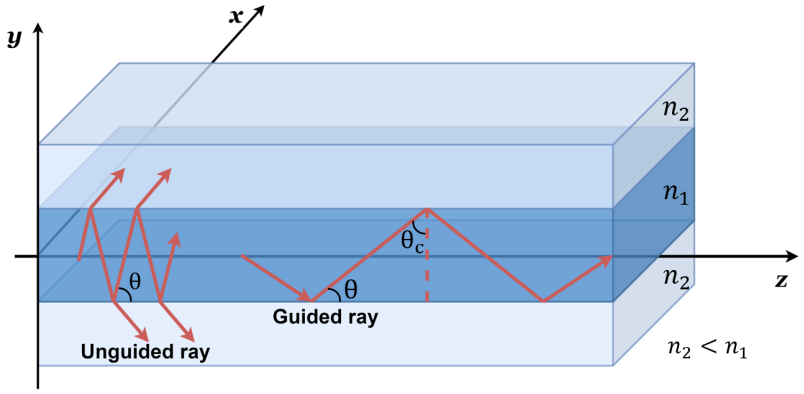

Figure 2.3: Basic planar dielectric slab waveguide with rays guided by total internal reflection. Media are assumed lossless. Dark blue is the core with refractive index n_1, light blue is the cladding with refractive index $n_2 < n_1$. Figure adapted from [5].

Light rays are guided in a dielectric medium, called the core, with refractive index n_1 placed between two layers of a medium called the cladding. The cladding has refractive index $n_2 < n_1$. For the waveguide to guide, the concept of total internal reflection must be achieved. Total internal reflection is defined by Snell's law in eq. 2.33 [5].

$$n_1 sin(\theta_1) = n_2 sin(\theta_2) \tag{2.33}$$

When the angle of reflection for the light rays θ shown in firgure 2.3 is smaller than the critical angle, total internal reflection is achieved. The critical angle θ_c is found by rearranging Snell's law as shown in eq. 2.34.

$$sin(\theta_c) = \frac{n_2}{n_1} \tag{2.34}$$

For the wave to propagate uniformly through the waveguide, it has to interfere constructively and destructively after being twice reflected. Imposing a self-consistency condition requiring that a twice reflected wave is equal to the non-reflected wave, gives two distinct waves. This self-consistency is dependent on the phase shift experienced by the wave when twice reflected, and a phase shift due to reflections [7]. Figure 2.4 shows the $\boldsymbol{k}$-vector diagram of a planar wave with wave vector k_0 in a waveguide where β_m is the z-component hence the propagation constant for the mode.

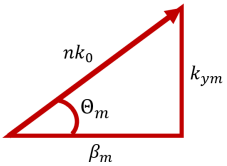

Figure 2.4: $\boldsymbol{k}$-vector diagram of a planar wave with wave vector k_0 in a waveguide.

Assuming a dielectric slab with a field in the form of a monochromatic TEM plane wave with the wave-vector components $k_x = 0$, $k_y = n_1 k_0 sin(\theta)$ and $k_z = n_1 k_0 cos(\theta)$, where the wave number is $k = n_1 k_0$, the self-consistency condition of dielectric waveguides is given in eq. 2.35. Here $\lambda = \lambda_0 / n_1$ is the wavelength, d is the width of the core, $\theta < \theta_c$ is the angle of reflection of the wave and is smaller than the critical angle θ_c, φ_r is the phase shift at the dielectric boundary, and m is the mode [5].

$$\frac{2\pi}{\lambda} 2d \cdot sin(\theta) - 2\varphi_r = 2\pi m \quad m = 0, 1, 2, \ldots \quad or \quad 2k_y d - 2\varphi_r = 2\pi m \tag{2.35}$$

A dielectric medium can also be represented by its relative permittivity, also called dielectric constant, which is represented as in eq. 2.36 where $\epsilon =$ is the electric permittivity in the medium and ϵ_0 is the electric permittivity in vacuum. The dielectric constant is useful in characterizing a dielectric material, which in an isotropic material is related to refractive index by $n^2 = \epsilon$.

$$\langle \epsilon \rangle = \frac{\epsilon}{\epsilon_0} \tag{2.36}$$

2.2.2 Modes in Dielectric Waveguides

As light travels through a waveguide, each reflection causes a phase shift without changing amplitude or polarization. According to [5], modes are fields that maintain the same transverse distribution and polarization at all locations along the waveguide axis. To determine the modes in a waveguide, the self-consistency condition from eq. 2.35 is imposed, where the modes are the fields that satisfy the condition in eq. 2.37 [5].

$$m = \frac{2d}{\lambda} sin(\theta) - \frac{\varphi_r}{\pi} = \frac{k_y d - \varphi_r}{\pi} \tag{2.37}$$

Using the TEM mode to describe Maxwell's equations is shown earlier, however, in waveguides there are more often transverse-electric (TE) or transverse-magnetic (TM) polarization and modes. TE polarization is when the *electric* field is orthogonal to the plane of incidence, while TM is when the *magnetic* field is orthogonal to the plane of incidence [4]. In the case of TE polarization in a waveguide, the electric field is oriented in the x-direction. Hence, the specific self-consistency condition for TE modes is shown in eq. 2.38.

$$tan\left(\pi \frac{d}{\lambda} sin(\theta) - m\frac{\pi}{2}\right) = \sqrt{\frac{sin^2(\theta_c)}{sin^2(\theta)} - 1} \tag{2.38}$$

The z-components of the TE polarized wave correspond to its propagation constant which can be presented as in eq. 2.39, where θ_m are the bounce angles of the mode m. The bounce angles are the angles at which the wave bounces on the barrier between the core and cladding and are restricted by the critical angle θ_c.

$$\beta_m = n_1 k_0 \cos\theta_m \tag{2.39}$$

There may be multiple TE or TM modes present in a waveguide. For a given frequency, the number of modes that can propagate through it is determined by its cutoff condition; the relationship between the frequency of the wave, the dimensions, and the material properties of the waveguide. The cutoff condition determines the minimum frequency at which a particular mode can propagate through the waveguide without significant loss or attenuation. To calculate the number of TE modes in a waveguide with core refractive index n_1 and cladding refractive index n_2, eq. 2.40 is used.

$$M \doteq \frac{2d}{\lambda_0} \sqrt{n_1^2 - n_2^2} \tag{2.40}$$

The equations for the self-consistency condition, propagation constant and number of modes for TM polarized waves are similarly obtained as for the TE polarized waves.

The theoretical presentation of modes in rectangular waveguides such as the ones further described below can be done using Marcatili's method or Effective index method and is more complex compared to a planar waveguide. Therefore, to calculate their modes, simulations with finite difference method or finite element method, are more often used [8].

2.2.3 Single-Mode Condition

When a waveguide only supports one mode, it is called a single-mode waveguide. This happens for a specific geometry for the waveguide, where either the thickness is very small or the wavelength is very long. A dielectric waveguide always supports the fundamental TE mode TE_{00}, hence this is the mode present in single-mode. From the self-consistency condition and mode calculations it is shown that the relations in eq. 2.41 ensure single-mode [5].

$$\frac{\lambda}{2d} > sin(\theta_c) \quad or \quad \frac{2d}{\lambda_0}\sqrt{n_1^2 - n_2^2} < 1 \tag{2.41}$$

Mode cutoff frequency can also be used to describe single-mode since the cutoff frequency is decided by the number of modes. The condition will then be eq. 2.42, where ν is the frequency of the wave and ν_c the mode cutoff frequency [5].

$$\nu > \nu_c = \frac{\omega_c}{2\pi} = \frac{1}{\sqrt{n_1^2 - n_2^2}}\frac{c_0}{2d} \tag{2.42}$$

For waveguide applications, single-mode is often used since distinguishing different modes when measuring transmission is difficult.

2.2.4 Confinement Factor

To measure light-matter interaction in a medium, the confinement factor Γ is used. It is used to quantify the extent to which light is confined within a particular medium in for instance an optical waveguide. Visser derived the confinement factor in [9] and Vlk further developed this in [7]. The following derivations are based on these sources and is thoroughly repeated as the concept is complex and central to the thesis.

The confinement factor is typically expressed as a percentage, with a higher confinement factor indicating a stronger interaction between light and matter and a greater degree of confinement. The confinement factor is an important parameter in the field of optics and is used to understand the behavior of light in different media, as well as to design and optimize optical devices and systems. Mathematically Γ is seen as a proportionality constant between the modal absorption coefficient α_m and bulk absorption coefficient α_i in eq. 2.43, where i is the different materials in a waveguide such as core, cladding and substrate.

$$\alpha_m = \sum_i \Gamma_i \alpha_i \tag{2.43}$$

To find Γ, Poynting's theorem, as previously shown in eq. 2.15, is used to represent the field through a two dimentional waveguide shown in eq. 2.44. It relates the energy density of volume V, to the power passing through the volume's surface S.

$$\iint_S (\mathbf{E} \times \mathbf{H}^*) \cdot \mathbf{n} dS = \iiint_V (j\omega\epsilon^* \mathbf{E} \cdot \mathbf{E}^* - j\omega\mu \mathbf{H} \cdot \mathbf{H}^*) dV \tag{2.44}$$

Furthermore, the field of a guided wave propagating in the z direction is given by eq. 2.45, where $\beta = \beta' - j\beta''$.

$$\mathbf{E}(x,y,z) = \tilde{\boldsymbol{E}}(x,y)e^{-j\beta z}, \quad \mathbf{H}(x,y,z) = \tilde{\boldsymbol{H}}(x,y)e^{-j\beta z} \tag{2.45}$$

β is related to the modal absorption α_m as in eq. 2.46.

$$\alpha_m = 2Im\{\beta\} \tag{2.46}$$

Assuming the flow of power is only in the z-direction the system is illustrated as in figure 2.5. For this system, the Poynting theorem above reduces to eq. 2.47, where $\mathbf{e}_z = (0,0,1)$.

$$\iint_S (\mathbf{E}\times\mathbf{H}^*)\cdot\mathbf{n}dS = -\iint_A (\mathbf{E}\times\mathbf{H}^*)\cdot\mathbf{e}_z dxdy + \iint_B (\mathbf{E}\times\mathbf{H}^*)\cdot\mathbf{e}_z dxdy \tag{2.47}$$

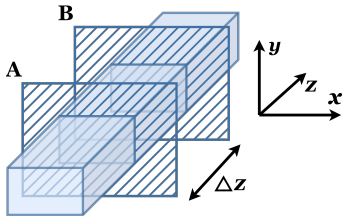

Figure 2.5: Diagram of a two dimensional waveguide with light propagation in the z direction. Surfaces A and B restrict the volume over which the integration is made. Adapted from [7].

It is shown that $(\mathbf{E}\times\mathbf{H}^*)$ increases by $e^{-\alpha_m\Delta z}$ between A and B. This gives the following simplification of eq. 2.44, eq. 2.48.

$$\iint_S (\mathbf{E}\times\mathbf{H}^*)\cdot\mathbf{n}dS = (e^{-\alpha_m\Delta z}-1)\iint_A (\tilde{\boldsymbol{E}}\times\tilde{\boldsymbol{H}}^*)\cdot\mathbf{e}_z dS \tag{2.48}$$

Moreover, using eq. 2.45 and the fact that the field is independent of z, the right hand side of eq. 2.44 is simplified as shown in eq. 2.49.

$$\begin{aligned} j\omega\iiint_V (\epsilon^*|\mathbf{E}|^2-\mu|\mathbf{H}|^2)dV &= j\omega\int_0^{\Delta z} e^{-\alpha_m z}dz\iint_A (\epsilon^*|\tilde{\boldsymbol{E}}|^2-\mu|\tilde{\boldsymbol{H}}|^2)dxdy \\ &= \frac{j\omega}{\alpha_m}(e^{-\alpha_m\Delta z}-1)\iint_A (\epsilon^*|\tilde{\boldsymbol{E}}|^2-\mu|\tilde{\boldsymbol{H}}|^2)dxdy \end{aligned} \tag{2.49}$$

Then, the combination of eq. 2.44, eq. 2.48 and eq. 2.49 gives eq. 2.50.

$$-\alpha_m\iint_A (\mathbf{E}\times\mathbf{H}^*)\cdot\mathbf{e}_z dS = j\omega\iint_A (\epsilon'|\tilde{\boldsymbol{E}}|^2-\mu|\tilde{\boldsymbol{H}}|^2)dxdy - \omega\iint_A \epsilon''|\tilde{\boldsymbol{E}}|^2 dxdy \tag{2.50}$$

Rearrangement for the modal absorption α_m is shown in eq. 2.51.

$$\alpha_m = \frac{\omega\iint_A \epsilon''|\tilde{\boldsymbol{E}}|^2 dxdy}{Re\{\iint_A(\tilde{\boldsymbol{E}}\times\tilde{\boldsymbol{H}}^*)\cdot\mathbf{e}_z dxdy\}} \tag{2.51}$$

Now, to obtain the general confinement factor Γ_i for material i, eq. 2.51 is incorporated into eq. 2.43. This is shown in eq. 2.52.

$$\sum_i \Gamma_i\alpha_i = \frac{\omega\iint_A \epsilon''|\tilde{\boldsymbol{E}}|^2 dxdy}{Re\{\iint_A(\tilde{\boldsymbol{E}}\times\tilde{\boldsymbol{H}}^*)\cdot\mathbf{e}_z dxdy\}} \tag{2.52}$$

Assuming the absorption coefficient of material i is given by $\alpha = 2n''k_0$, and that the permittivity $\epsilon = \epsilon_r\epsilon_0$ of the material has the relative permittivity $\epsilon_r = (n'-jn'')^2$, it is given that $\epsilon_r'' = 2n'n''$. The simplification of eq. 2.52 then becomes eq. 2.53.

$$\sum_i \Gamma_i \alpha_i = 2k_0 c\epsilon_0 \frac{\iint_A n' n'' |\tilde{\boldsymbol{E}}|^2 dxdy}{Re\{\iint_A (\tilde{\boldsymbol{E}} \times \tilde{\boldsymbol{H}}^*) \cdot \mathbf{e}_z dxdy\}} \tag{2.53}$$

In optical waveguides, it is common to have separate media with constant n_i' and n_i''. This allows isolation of α_i and adjustment of the integration limits in eq. 2.53, giving eq. 2.54.

$$\sum_i \Gamma_i \alpha_i = \sum_i \alpha_i c\epsilon_0 n' \frac{\iint_A |\tilde{\boldsymbol{E}}|^2 dxdy}{Re\{\iint_A (\tilde{\boldsymbol{E}} \times \tilde{\boldsymbol{H}}^*) \cdot \mathbf{e}_z dxdy\}} \tag{2.54}$$

Rearranging for Γ_i gives eq. 2.55.

$$\Gamma_i = \frac{c\epsilon_0 n_i' \iint_i |\tilde{\boldsymbol{E}}|^2 dxdy}{Re\{\iint_{-\infty}^{\infty} (\tilde{\boldsymbol{E}} \times \tilde{\boldsymbol{H}}^*) \cdot \mathbf{e}_z dxdy\}} \tag{2.55}$$

This is the representation of confinement factor often used. However, a simpler, more intuitive formula can be derived using the group velocity v_g of the travelling wave in the medium. Equation 2.56 shows v_g represented using the Poynting vector.

$$Re\left[\iiint_{-\infty}^{\infty} (\tilde{\boldsymbol{E}} \times \tilde{\boldsymbol{H}}^*) \cdot \mathbf{e}_z dxdy\right] = v_g \iiint_{-\infty}^{\infty} \epsilon |\tilde{\boldsymbol{E}}|^2 dxdy \tag{2.56}$$

Incorporating eq. 2.56 into eq. 2.55, gives eq. 2.57.

$$\Gamma_i = \frac{n_g}{n_i} \frac{\iint_i \epsilon |\tilde{\boldsymbol{E}}|^2 dxdy}{\iint_{-\infty}^{\infty} \epsilon |\tilde{\boldsymbol{E}}|^2 dxdy} \tag{2.57}$$

A modification of Lambert-Beer law gives the absorption along the waveguide length as in eq.2.58.

$$I = I_0 e^{-\alpha \Gamma L} \tag{2.58}$$

2.2.5 Optical Waveguide Geometries and their Properties

The two-dimentional, rib and strip waveguides are common waveguide geometries used in optics.

Two-Dimensional Dielectric Waveguides confine light in both the x and y directions; two transverse directions. This means the dielectric core of the waveguide is surrounded by cladding on all sides. Using the simplest two-dimensional dielectric waveguide, a rectangular waveguide, the wave vector (k_x, k_y, k_z) of the light is therefore confined by eq. 2.59. A figure of the rectangular dielectric waveguide is seen in figure 2.6.

$$k_x^2 + k_y^2 \leq n_1^2 k_0^2 sin^2(\theta_c) \tag{2.59}$$

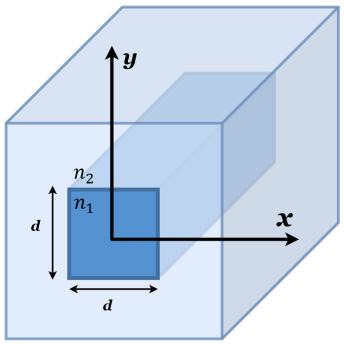

Figure 2.6: Two-dimensional rectangular dielectric waveguide with cladding in light blue with refractive index n_2 and dielectric core in dark blue with refractive index n_1. d is the thickness of the core. Adapted from [5].

The Strip Waveguide is a common geometry for a two-dimensional dielectric waveguide. Figure 2.9 shows a simple illustration of a strip waveguide where s is the strip height and w is the width of the strip.

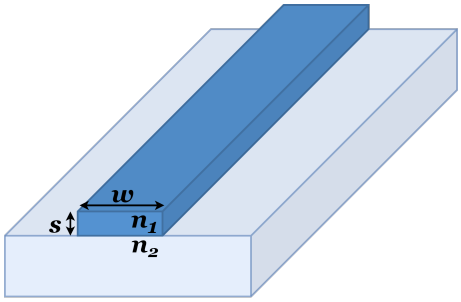

Figure 2.7: Simple strip waveguide with cladding in light blue with refractive index n_2 and dielectric core in dark blue with refractive index n_1. Adapted from [5].

The strip waveguide lays as a strip on top of the cladding. By changing the strip's height and width, one can change the characteristics of the propagating wave. The design is often used in waveguide optics as it has high field confinement, low signal loss and can have dimensions in the nanometer scale. However, their biggest advantage is their ability to support single-mode propagation.

According to [7], figure 2.8 shows field distributions in a strip waveguide for TE_{00} and TM_{00} modes. It shows how the field is well confined within the strip for TE mode, and has a small evanescent field for TM mode. Overall there is some loss, but it is low.

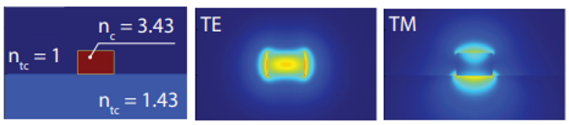

Figure 2.8: Electric field distributions for TE_{00} and TM_{00} modes in a strip waveguide. The waveguide's geometry is shown to the left. Adapted from figure in [7].

The Rib Waveguide is another common geometry for a two-dimensional dielectric waveguide. Figure 2.9 shows a simple illustration of a rib waveguide where h is the height of the waveguide, s is the strip height and w is the width of the strip.

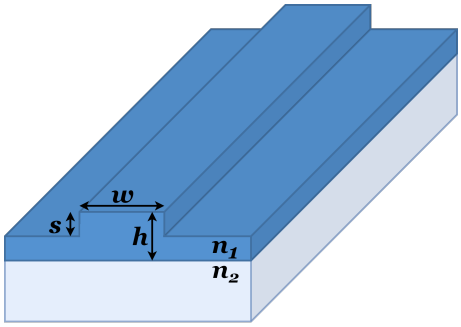

Figure 2.9: Simple rib waveguide with cladding in light blue with refractive index n_2 and dielectric core in dark blue with refractive index n_1. Adapted from [5].

The rib waveguide is different from the strip waveguide in that the dielectric core is not etched all the way down to the cladding. The result is a rib on a larger dielectric slab. Its characteristics are more versatile than the strip as the combination of changing h, s and w gives a larger design space and possibilities to fine tune i.e. modes, loss and intensity. The rib design also reduces loss that might appear on the etched sides of a strip waveguide, while still confining the electromagnetic field. Rib waveguides are often used in applications where light matter interactions are interesting. Similar to strip waveguides, rib waveguides are also often used in optics due to their ability for single-mode propagation, small size, low loss and high confinement.

According to [7], figure 2.10 shows field distributions in a rib waveguide for TE_{00} and TM_{00} modes. Differently from the strip waveguide, there is now a much wider field for both TE and TM modes due to the slab waveguide below the rib.

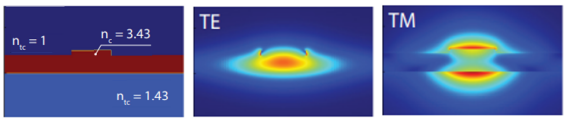

Figure 2.10: Electric field distributions for TE_{00} and TM_{00} modes in a rib waveguide. The waveguide's geometry is shown to the left. Adapted from figure in [7].

2.2.6 Losses in Waveguides

Waveguides experience several different types of loss i.e. *absorption losses, scattering losses, leakage to the substrate, bending losses* and *coupling losses*. Generally loss is found from the propagation constant β and the loss units are (dB/cm) and (dB/rad).

Absorption losses are dependent on the material of the waveguide and how light is allowed to propagate in it. The losses are due to absorption of energy into the material and are dependent on permittivity and conductivity of the waveguide, as well as dimensions and frequency. Oxides are examples of materials that often have little absorption and are therefore beneficial for waveguides.

The absorption coefficient α is often used to calculate absorption losses, as the intensity of a wave is proportional to $e^{-\alpha z}$. It can also be represented using the following equation 2.60, where P_i is the input power and P_t is the transmitted power of the wave [7].

$$L = 10 \log \frac{P_i}{P_t} \tag{2.60}$$

Scattering loss can both be due to electron-collisions within the waveguide material or scattering at the boundary between waveguide and cladding, i.e. refraction. It can be caused by a variety of factors, such as surface roughness, defects, or inhomogeneities in the waveguide material. It can also be caused by the interaction of the electromagnetic wave with the atomic or molecular structure of the waveguide material. At high frequencies and small wavelengths, scattering loss is more prominent. This is due to the frequent fluctuation of the wave giving a higher risk of reflection angles larger than the critical angle θ_c. A larger cross-sectional area in a waveguide for instance, may reduce scattering loss [7].

Leakage to the substrate is occurring when the cladding of a waveguide is deficient in isolating the guided wave from the substrate. The evanescent field extends through the cladding and into the substrate, causing loss. For such leakage to occur, the refractive index of the substrate must be larger than the effective index of the guided wave. To avoid this type of loss one can therefore either increase cladding thickness or use a substrate with low refractive index [7].

Bending losses are due to the curvature or the bending of the waveguide. The electromagnetic field propagation depends on the waveguide geometry and for a bent waveguide, this includes the bending radius R and the angle of the bend θ shown in figure 2.11 [10].

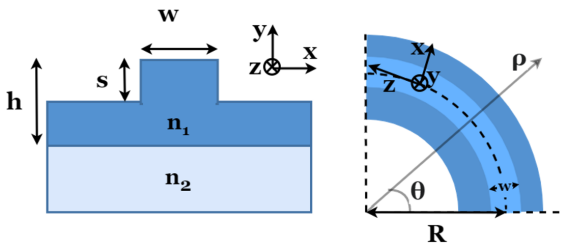

Figure 2.11: Illustration of bending radius R in a rib waveguide with angle of the bend θ, cladding in light blue with refractive index n_2 and dielectric core in dark blue with refractive index $n_1 > n_2$. h is the height of the waveguide, s is the strip height and w is the width of the waveguide. Adapted from [10].

For a straight waveguide, assuming single mode, the field can be represented in the form shown in eq. 2.61 where β is the propagation constant.

$$\mathbf{E}(x,y,z) = \tilde{\boldsymbol{E}}(x,y)e^{i\beta z}, \quad \beta = k_0 n_{eff} \tag{2.61}$$

Comparably, for a bent waveguide, the field can be represented in the cylindrical form shown in eq. 2.62 with a propagation constant β^*. Here the dependability on the bending radius R and angle of the bend θ is visible. The unit for the bending loss is (dB/rad) [11].

$$\mathbf{E}(\rho,\theta,y) = \tilde{\boldsymbol{E}}(\rho,y)e^{i\beta^*\theta}, \quad \beta^* = k_0 n_{eff} R \tag{2.62}$$

The goal for waveguide sensors is minimal bending losses while ensuring a single-mode waveguide [10]. Hence, patterning of bent waveguides is carefully designed with optimal bending. An example of a design of a bent waveguide for low bending losses uses Euler-curve S-bend. It is defined in eq. 2.63 where L is the length of the curve, $A = [L_{max}/(1/R_{min} - 1/R_{max})]^{1/2}$ and L_{max} is the total length of the bend [12].

$$\frac{d\theta}{dL} = \frac{1}{R} = \frac{L}{A^2} + \frac{1}{R_{max}} \tag{2.63}$$

Coupling losses are relevant when coupling waveguides together, either parallel or in series. Reasons for the loss may be poor mode matching, slight differences in geometry or phase shifts. Coupling losses are also relevant when arranging waveguides into for instance spirals. Here, the goal is to avoid coupling between the circles in the spiral and can be improved by ensuring large enough gaps between them. Below is a more thorough explanation of coupling into optical waveguides.

2.2.7 Coupling into Optical Waveguides

When working with dielectric optical waveguides, light is coupled from a light source into the waveguide. Coupling is the process of transferring light energy from an optical component to another and can be done between optical fibers, waveguides and photonic devices. The process depends on mode matching which is when the modes of the two devices included in the coupling, are the same. Mode matching involves that the transverse distribution of the incident light matches the mode of the receiving component. Figure 2.12 shows an illustration of the coupling between a lensed optical fiber and an optical planar waveguide. The source power distribution $s(y)$ must match the waveguide's mode distribution $u(y)$. In this case, the lens on the fiber is used to collimate the light to achieve a more precise beam [5].

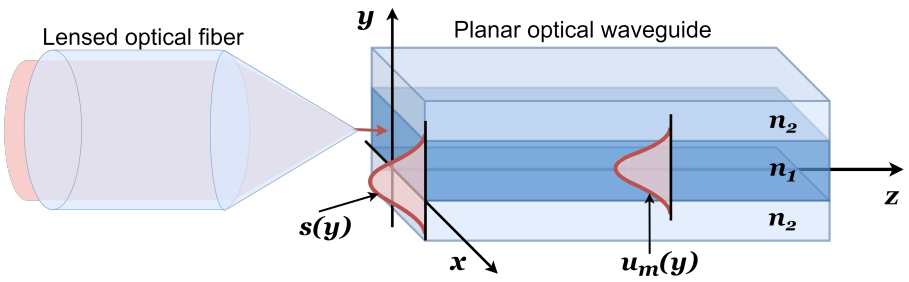

Figure 2.12: Coupling between a lensed optical fiber with source power distribution $s(y)$ and an optical planar waveguide with mode distribution $u(y)$. Adapted from [5].

The light from the source must also be emitted within the angle of acceptance of the receiving component. In the case in figure 2.12, the angles of the guided waves within the waveguide are characterized by the previously mentioned Snell's law and can be written as in equation eq.2.64.

$$\theta_c = sin^{-1}\frac{n_2}{n_1} \tag{2.64}$$

The angle of acceptance θ_a is defined from the numerical aperture NA shown in equation 2.65.

$$NA = sin\theta_a = n_1 sin\theta_c = n_1\sqrt{1-\left(\frac{n_2}{n_1}\right)^2} = \sqrt{n_1^2 - n_2^2} \tag{2.65}$$

This gives the angle of acceptance θ_a shown in 2.66.

$$\theta_a = sin^{-1}\left(\sqrt{n_1^2 - n_2^2}\right) \tag{2.66}$$

Figure 2.13 illustrates the relation between the angle of acceptance θ_a and critical angle θ_c in a planar waveguide.

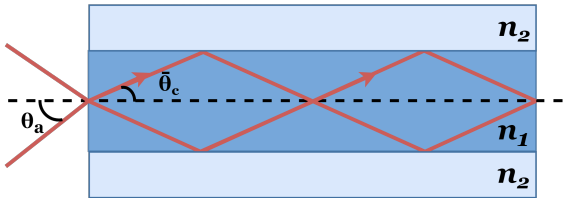

Figure 2.13: Illustration of the relation between the angle of acceptance θ_a and critical angle θ_c in a planar waveguide. Adapted from [5].

Efficient coupling can be achieved by choosing optical components that collimate the beam from the light source, such as the lensed optical fiber in figure 2.12. The predominant technique is butt coupling, which involves aligning the end faces of waveguides or fibers. However, other methods such as prism couplers and grating couplers can also be used for efficient light transfer and are further explained in [5].

2.3 Effective Medium Approaches to Calculate Porosity

A mesoporous medium will, due to the two different materials present in the medium, have a different electric permittivity and dielectric constant than the same non mesoporous medium. Furthermore, the refractive index and confinement factor of the medium will be affected by the porosity since the propagation of the field in the medium is affected by the different dielectric constants. Schwarz et al. summarize in [13], the relation between these characteristics in a mesoporous medium using the effective medium approach by Lorentz and Lorenz, as well as the effective medium approximation by Bruggeman [14]. Schwarz et al.'s summary is further denoted here.

The characteristics of a mesoporous material are described by its dielectric function $\langle\epsilon\rangle$. From the Clausius-Mossotti relation, which assumes homogeneous spherical pores homogeneously distributed in a dielectric medium, the dielectric constant of the spherical particles $\langle\epsilon\rangle$ is related to their density N and polarization α by eq. 2.67 [15].

$$\frac{\langle\epsilon\rangle - 1}{\langle\epsilon\rangle + 2} = \frac{N\alpha}{3\epsilon_0} \tag{2.67}$$

In a medium with more than one material with different densities and polarizabilities, these are summarized for the total dielectric function of the mixed material, shown in eq. 2.68.

$$\frac{\langle\epsilon\rangle - 1}{\langle\epsilon\rangle + 2} = \frac{1}{3\epsilon_0}\sum_i N_i\alpha_i \tag{2.68}$$

In case of a gas with $\epsilon_g \approx 1$, such as air, equation 2.69 simplifies the above expression [15].

$$\epsilon_g = 1 + \frac{N_g\alpha_g}{\epsilon_0} \tag{2.69}$$

Finally, the change in dielectric constant in a mesoporous material with the addition of a gas with polarizability α_g and the density N_g is described by Lorentz-Lorenz in equation 2.70. Here the dielectric function of the non mesoporous part of the material is ϵ_m and the porosity of the material is p.

$$\frac{\langle\epsilon\rangle - 1}{\langle\epsilon\rangle + 2} = (1-p)\frac{\epsilon_m - 1}{\epsilon_m + 2} + p\frac{\epsilon_g - 1}{\epsilon_g + 2} \tag{2.70}$$

Equation 2.71 shows eq. 2.70 rearranged for $\langle\epsilon\rangle$.

$$\langle\epsilon\rangle = \frac{2p\epsilon_g + \epsilon_g\epsilon_m - 2p\epsilon_m + 2\epsilon_m}{\epsilon_g + p(\epsilon_m - \epsilon_g) + 2} \tag{2.71}$$

This can be compared to the Bruggeman effective medium approximation for the same assumed mesoporous material with spherical pores shown in eq. 2.72.

$$0 = (1-p)\frac{\epsilon_m - \langle\epsilon\rangle}{\epsilon_m + 2\langle\epsilon\rangle} + p\frac{\epsilon_g - \langle\epsilon\rangle}{\epsilon_g + 2\langle\epsilon\rangle} \tag{2.72}$$

In the paper [13], it is concluded that by comparing the linearization coefficients of the two equations, "the Lorentz-Lorenz equation can only be safely quantitatively applied for very mesoporous materials ($p \approx 0.7$) in porosimetry studies." Hence, the Bruggeman approach should be used for less mesoporous materials with $p < 0.7$. From the approximations, it can be concluded that for a mesoporous material with spherical pores filled with gas with low dielectric constant (lower than the dielectric constant of the non mesoporous material), a higher porosity gives a total lower dielectric constant in the mesoporous material, than in the same non mesoporous material.

Chapter 3

Methods

The following chapter outlines established methods utilized in simulation, fabrication and characterization of mesoporous optical waveguides respectively. Chapter 4 later explains the experimental procedures followed using these methods and theory from Chapter 2.

3.1 Simulation Methods

Simulations of the mesoporous optical waveguides were performed using the MODE solver from Ansys Lumerical. The tool is recognized as having fast and reliable calculations and has been known to be used in similar research such as in [7] and [1]. The MODE solver uses a finite difference eigenmode (FDE) solver to calculate the field distribution in a simulated waveguide. The solver also allows for simulation of a bent waveguide, as well as specific boundary conditions such as perfectly matched layers (PMLs). The PMLs can be used for loss analysis [16]. Below are methods used in Ansys Lumerical for this thesis; the Finite Difference Eigenmode Method in section 3.1.1, mesh optimization in section 3.1.2 and the method for calculation of confinement factor in section 3.1.3. More detailed descriptions of Ansys Lumerical's MODE solver can be found in their documentation [17].

3.1.1 Finite Difference Eigenmode (FDE) Method

The finite difference method is a technique used to solve partial differential equations by approximating derivatives with finite difference approximations on a discrete grid. When estimating electromagnetic fields on a cross section, the grid consists of $\boldsymbol{E}$ and $\boldsymbol{H}$ field approximations. The Ansys Lumerical MODE solver uses the Yee's 2D mesh grid in its simulations [16] [18]. In Yee's mesh Maxwell's equations are substituted with a set of finite difference equations in a cross sectional mesh [19]. The mesh size and fineness sets the boundaries of the equations.

3.1.2 Mesh Optimization

In order to ensure appropriate mesh size for calculations in Ansys Lumerical, convergence testing for optimization is useful. As a smaller mesh size will allow for more accurate estimations of field distributions, the simulation time and memory requirements limit the size [16]. Convergence testing of mesh is done to ensure the smallest mesh suitable for efficient simulations. It is simply done by simulation using different mesh sizes and different fineness of mesh and analysing the results of the calculations. The results should converge around the optimal mesh size.

3.1.3 Confinement Factor Calculation

As outlined in section 2.2.4, the confinement factor gives a measurement of light-matter interaction in a medium in a waveguide and is useful in determining the sensitivity of an optical mesoporous waveguide. To calculate the predicted confinement factor of the mesoporous waveguides studied in this report a script developed by Vlk in [7] was utilized and altered. The final, edited, script is found in appendix A. It uses parameters of the fundamental mode of the rib waveguide given by the modal analysis performed in Ansys Lumerical MODE solver.

In the script a binary mask to define the confinement region is created using a mask-matrix. The field data is retrieved at the respective axis, the mask is applied, and the data is added into the equation for confinement factor by integrating according to the equation outlined in 2.57. Finally, the confinement factor is printed as percentage in the programs script output.

3.2 Fabrication Methods

The mesoporous optical waveguides were fabricated using the Sol-gel method in December 2022 by Sebastián Alberti. As part of my thesis work, microfluidic cells were fabricated using PDMS. The microfluidic cells will be used to introduce solvents onto the mesoporous waveguide to subsequently characterize the waveguide's spectroscopic response to solvents. The following sections 3.2.1 and 3.2.2 describe the Sol-gel method and the method for PDMS fabrications respectively.

3.2.1 Sol-gel Method for Mesoporous Waveguides

The sol-gel method is a well established method for thin film optics that allows for tunable porosity. The method is therefore well suited for fabrication of mesoporous optical waveguides. This section aims to summarize the basic chemistry behind the sol-gel method and outline the steps required in its fabrication [20].

To start, a precursor is chosen and prepared. The most common precursors are generally alkoxides or halides. These are dissolved in solvents with low surface tension and sometimes acid or a chelating agent to stabilize the solution and control the condensation process. To achieve hybrid materials, such as mesoporous waveguides, organic modified silica silanes with a polymerizable group or monomers may also be added. After preparing the sols, they are often either spin coated or dip coated on glass, silicon or conductive substrates. Figure 3.1 shows the sol-gel process schematically represented from [21]. In the case of mesoporous waveguides such as the one in this report, spin coating is typically used [20].

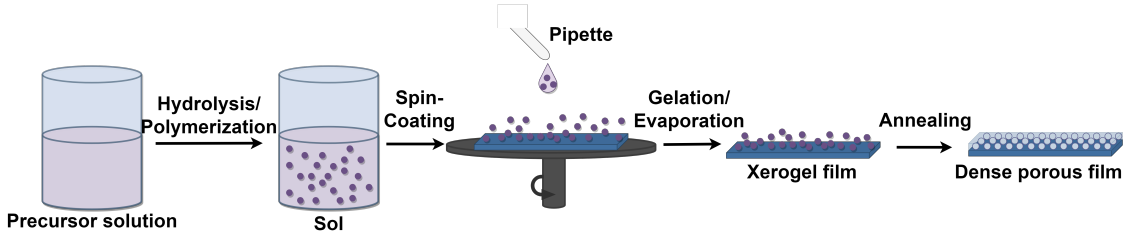

Figure 3.1: Schematic representation of sol-gel method adapted from [21].

The thin film can be fabricated to be between 20nm to 500nm which is adjusted by modifying conditions of the sols, such as viscosity and density. To avoid cracking that might happen when fabricating thicker layers due to the high mechanical stress, it is possible to develop multiple thin layers to achieve a thick mesoporous layer. This may, on the other hand, compromise the structural uniformity of the pores due to the connectivity of pores between the layers. Following spin coating, the sample is post processed, normally using heat treatment. Depending on the temperature, calcination is often achieved and is used for template removal, leaving pores in the thin film. This leaves a thin mesoporous film ready for patterning. Standard top down lithography can be used on sol-gel layers in order to pattern them, making them very versatile [20].

3.2.2 PDMS fabrication

Polydimethylsiloxane (PDMS) is often used when working with microfluidics such as in [22]. It is a flexible, chemically stable and non-invasive material. The polymer is based on silicon and can easily be molded to any shape using lithography or by cutting after hardening. In this

project, PDMS is used to fabricate microfluidic cells to contain liquid solutions on the interface of mesoporous waveguides. C.W. Tsao describes the method of PDMS fabrication in [23] and it is briefly recounted here.

Casting PDMS is done by mixing a 10:1 ratio of Polydimethylsiloxane base and reagent allowing it to start curing. Curing is done at 60-80°C for 2-4 hours depending on the sample size. The casting can be performed in a master micromold made with soft lithography, or in a basic dish. After curing, the PDMS layer can be removed from its mold and treated to seal onto desired surfaces, samples or chips. Treatments include enhancing bonding strength by oxygen plasma treatments. However, due to van der Waals forces, the PDMS can be reliably stuck to another PDMS sample or glass substrates without the need for additional treatment, and is the procedure followed in this thesis.

3.3 Characterization Methods

To characterize the fabricated mesoporous optical waveguide, methods of ellipsometry and near infrared transmission measurements were applied. Ellipsometry is a recognised method for thin film property characterization used by [24] among others. NIR transmission measurements are performed in a laser setup and provide spectral information on the waveguide's transmission abilities and propagation properties. Section 3.3.1 provides an elaboration on the ellipsometry method, while section 3.3.2 gives an overview of methods used in analysis of spectra from transmission measurements, as well as an overview of retrieved absorption spectra of liquids used in measurements.

3.3.1 Ellipsometry

Ellipsometry is a method used for measurements on thin film applications such as thin film waveguides as explored in [24]. It is based on optical reflectance and is sensitive and non-destructive. The method can be used for measurements of refractive index, thickness, conductivity and porosity and is therefore very versatile. Figure 3.2 shows an illustration of a basic ellipsometer adapted from [25].

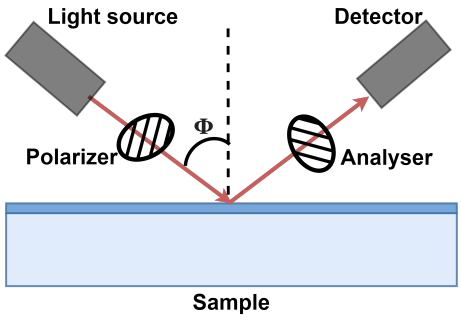

Figure 3.2: Simple illustration of ellipsometer adapted from [25].

The device consists of a light source, a detector, a polarizer and an analyser. The light source is typically a monochromatic single-wavelength laser, while the detector is typically a photodiode or a photomultiplier tube. In short, ellipsometers use the change in polarization state of light reflected on a sample surface. This is measured by comparing the amplitude ratios of two perpendicularly polarized beams at a variable angle of incidence ϕ. When working with isotropic, non-absorbing layers, a single wavelength is typically utilized in the measurement process. On the other hand, for more complex structures the wavelength is scanned over a broad range. This is called spectroscopic ellipsometry [25].

Schubert gives a detailed description of the theory behind spectroscopic ellipsometry in the book Handbook of Ellipsometry [26]. The following is a short summary of his outline of a polarized ellipsometer which is a common type of ellipsometer for thin film layers on top of other materials.

Generalized, the approach for a polarized ellipsometer is to illuminate the sample with first one polarization p, and then another polarization s without changing the input. Then a measurement on how much p-polarised light converts to s-polarized light shows characteristics of the illuminated sample by using its electromagnetic field components. An analysis of the polarization change in the light at the output is then made using Jones matrices that explain the electromagnetic field components in a sample. The mathematical explanation of a Jones matrix will not be shown here as a conceptualized explanation is more relevant in this thesis.

Figure 3.3 shows a plane wave with plane of incidence p and s, and angle of incidence ϕ_a. A_p and A_s are the complex amplitudes of the p and s modes before reflection. B_p and B_s are the complex amplitudes of the p and s modes after reflection.

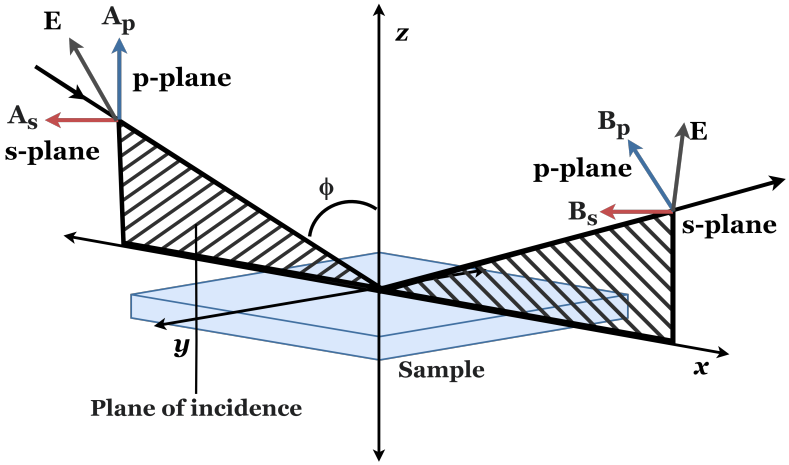

Figure 3.3: Plane wave with photon energy E, plane of incidence p and s, and angle of incidence ϕ_a. Complex amplitudes before and after reflection are A_p, A_s, B_p and B_s. Adapted from [26].

The illumination of the polarized plane wave gives a reflected and a transmitted plane wave. The complex amplitudes shown in the figure above, are related by the Jones matrices of the reflection $\boldsymbol{r}$ and transmission $\boldsymbol{t}$ waves as shown in eq. 3.1 and 3.2, where C_p and C_s are the modes of the transmitted beam.

$$\begin{pmatrix} B_p \\ B_s \end{pmatrix} = \boldsymbol{r} \begin{pmatrix} A_p \\ A_s \end{pmatrix} \tag{3.1}$$

$$\begin{pmatrix} C_p \\ C_s \end{pmatrix} = \boldsymbol{t} \begin{pmatrix} A_p \\ A_s \end{pmatrix} \tag{3.2}$$

Furthermore, Schubert shows that the complex reflectance ratio ρ and transmittance ratio τ can be used to normalize the Jones matrix elements in $\boldsymbol{r}$ and $\boldsymbol{t}$ as bilinear transformations. ρ and τ are defined as in eq. 3.3 and eq. 3.4. Here $\tan\Psi$ is the magnitude of the reflectivity or transmittance ratio and Δ is the phase difference between the reflected and transmitted p and s polarized light.

$$\rho \equiv \tan\Psi e^{i\Delta} \equiv (\frac{A_p}{A_s})^{-1}(\frac{B_p}{B_s}) \tag{3.3}$$

$$\tau \equiv \tan\Psi e^{i\Delta} \equiv (\frac{A_p}{A_s})^{-1}(\frac{C_p}{C_s}) \tag{3.4}$$

The normalization of the elements of the Jones matrices, give three complex parameter ratios for reflectance and three complex parameter ratios for transmittance. These ratios have common corresponding values of Ψ and Δ; Ψ_{pp}, Ψ_{ps}, Ψ_{sp}, Δ_{pp}, Δ_{ps} and Δ_{sp}. Ultimately, these real valued quantities are used for the ellipsometry data format. Often the formats $\tan\Psi$ and $\cos\Delta$ are used.

After performing measurements, the spectroscopic ellipsometer's software will present a graph of $\tan\Psi$ versus wavelength λ as well as one with $\cos\Delta$ versus wavelength. These graphs are then used in a best-fit calculation using a dispersion model relevant for the sample investigated. The model can also be adjusted in the software. After finding the model of best-fit

and ensuring a coefficient of determination close to 1, the thickness and refractive index are calculated from the model.

To calculate porosity of a sample, it is placed in an additional humidity or gas regulated chamber. The humidity is changed step wise and measurements done after every step, giving an overview of change in refractive index and layer thickness. This is used to calculate the porosity using one of the effective medium approaches explained in section 2.3.

3.3.2 NIR Spectral Analysis

Characterization of and measurements on optical waveguides may be done using near infrared (NIR) spectroscopy and spectral analysis. By exploiting the principles of absorption, emission, or scattering of light, optical spectroscopy provides insights into characteristics of materials. The data often received from optical spectra is absorbance or transmission. The equation for absorption A is repeated in eq. 3.5, where I_0 is the incident light, I the transmitted intensity, α is the absorption coefficient, C is the concentration and L is the pathlength of the sample.

$$A = log\frac{I_0}{I} = \alpha \times C \times L \tag{3.5}$$

Transmission is then found as in equation 3.6.

$$T = \frac{I}{I_0} \tag{3.6}$$

Finally, the absorption coefficient can be defined in relation to the imaginary part of complex refractive index k as shown in eq. 3.7.

$$\alpha = \frac{4\pi k}{\lambda} \tag{3.7}$$

Depending on the spectrum, different methods are used in order to analyse them. Some of the methods specifically used for near infrared laser spectroscopy are outlined below, as these methods are useful in processing results in this thesis. The theory is retrieved from Chapter 3 in B. Stuart's book Infrared Spectroscopy: Fundamentals and Applications [27].

Near infrared light covers the wavelength range of 780–2526nm and is a useful range for sensing technologies as it makes for non destructive and non invasive applications. To analyse transmission spectra from NIR measurements, different ways of spectrum manipulation can be engaged. Firstly, *baseline correction* is used by establishing a new baseline by connecting the points of minimum absorbance on a peak, preferably flat sections. The difference in absorbance between the new baseline and the maximum point of a peak or a band is then used. Furthermore, *smoothing* is a technique used to eliminate or reduce noise by blending features of the spectrum into each other. One smoothing function is the Savitzky-Golay filter. The method uses convolution and fits successive sets of adjacent data points with a polynomial by linear least squares and was published by A. Savitzky and M. J. E. Golay in 1964 [28]. Interpolation is another method that may be used in analysis and processing of spectra. In the book Python Programming and Numerical Methods [29], different interpolation methods are explained, including linear and spline interpolation. Linear interpolation is performed by estimation of a point on the line between existing data points. Hence, the datapoints are assumed to be linearly connected. Spline interpolation, or cubic spline, interpolates with a set of piecewise cubic functions. The data is assumed to be joined by a cubic polynomial, hence interpolation using this method is useful when working with polynomial spectra.

3.3.3 Absorption Spectra of Water, Ethanol and Methanol

In this thesis, a selected group of solvents are used in measurements; water, ethanol and methanol. The solvents were selected due to the safety declarations already in place in the lab. Ideally, the solvents or fluids used in transmission measurements in this thesis should have had distinct peaks in the wavelength range under investigation (1400-1600nm). Unfortunately, the identification of fluids with this characteristic that could safely be incorporated in the lab was unsuccessful, despite extensive literature searches and consolation with spectroscopists at the Norwegian University of Life Sciences (NMBU).

In order to analyse results of transmission measurements using the solvents, familiarization of the solution spectra is useful. Below is an overview of these spectra in the NIR range used in the transmission measurements. Figure 3.4 shows the calculated absorption coefficient in the NIR range of the water spectrum determined by M. Hale and R. Querry in [30] and the calculated absorption coefficient spectrum of ethanol and methanol in the NIR range from the imaginary refractive index k spectra retrieved from T. L. Myers et al.'s analysis in [31]. The data was plotted using MatLab and the equation for absorption coefficient in eq. 3.7.

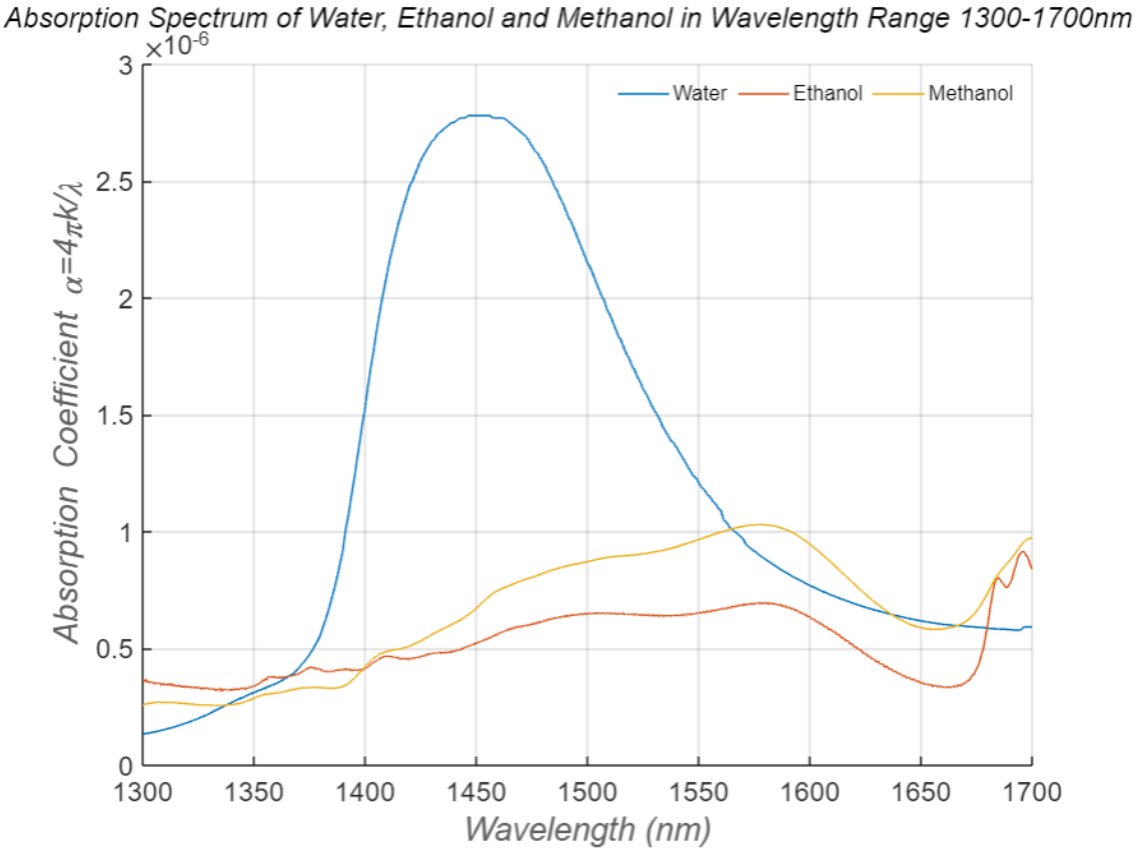

Figure 3.4: Absorption spectrum of water (blue), ethanol (red) and methanol (yellow) in the wavelength range 1300nm-1700nm calculated from complex refractive index data in courtesy of [30] and [31].

The water spectrum shows a peak of $\alpha_{water} = 2.8 \times 10^{-6}$ at $\lambda = 1450nm$, while the ethanol spectrum shows a peak at $\lambda = 1581nm$ of $\alpha_{ethanol} = 6.9 \times 10^{-7}$, and a small peak of $\alpha_{ethanol} = 6.5 \times 10^{-7}$ at $\lambda = 1500nm$. Similarly to ethanol, the methanol spectrum shows a peak at $\lambda = 1578nm$, but with maximum absorption coefficient of $\alpha_{methanol} = 1.1 \times 10^{-6}$,

and a small peak at $\lambda = 1500nm$ with $\alpha_{methanol} = 8.7 \times 10^{-7}$. At the wavelength used in simulations $\lambda_{sim} = 1550$, the absorption coefficient of water is $\alpha_{water1550} = 1.2 \times 10^{-6}$, the absorption coefficient of ethanol is $\alpha_{ethanol1550} = 6.5 \times 10^{-7}$ and the absorption coefficient of methanol is $\alpha_{methanol1550} = 9.7 \times 10^{-7}$. An overview of the different absorption coefficients outline here is shown in table 3.1.

Table 3.1: Highlighted absorption coefficients observed in the spectra in figure 3.4.

Solution	**Trait**	**Wavelength λ (nm)**	**Absorption coefficient α**
Water	Peak	1450	$\alpha_{water} = 2.8 \times 10^{-6}$
Ethanol	Peak	1581	$\alpha_{ethanol} = 6.9 \times 10^{-7}$
Ethanol	Peak	1500	$\alpha_{ethanol} = 6.5 \times 10^{-7}$
Methanol	Peak	1578	$\alpha_{methanol} = 1.1 \times 10^{-6}$
Methanol	Peak	1500	$\alpha_{methanol} = 8.7 \times 10^{-7}$
Water	Simulation λ	1550	$\alpha_{water} = 1.2 \times 10^{-6}$
Ethanol	Simulation λ	1550	$\alpha_{ethanol} = 6.5 \times 10^{-7}$
Methanol	Simulation λ	1550	$\alpha_{methanol} = 9.7 \times 10^{-7}$

The absorption in water is almost an order of magnitude higher than ethanol and methanol in this wavelength range. The absorption of methanol is 0.41 higher than of ethanol in this range.

Chapter 4

Experimental Procedures

The experimental procedures to investigate the possibilities for liquid sensing using mesoporous optical waveguides were derived from synthesis of the methods outlined in Chapter 3 and the theoretical background in Chapter 2. This chapter consists of the procedures followed for simulation in section 4.1, fabrication in section 4.2 and characterization in section 4.3 of a mesoporous optical waveguide respectively. Simulations were performed to investigate the confinement factor of mesoporous waveguides in relation to porosity, as well as to compare the confinement factor of the waveguide in different solutions. The calculations were done using the Ansys Lumerical MODE solver. Fabrication of the mesoporous waveguide was conducted using the Sol-gel method to obtain a porous material. Following, a microfluidic cell was fabricated using Polydimethylsiloxane (PDMS) to contain liquid on the waveguide sample. Characterization of the mesoporous optical waveguide was executed using ellipsometry and transmission measurements in a NIR tunable laser setup. The ellipsometry measurements aim to reveal the thickness, refractive index and porosity of the sample, while the transmission measurements were performed to measure the transmission spectrum of the mesoporous waveguide with different solutions as top cladding. The absorption was thus calculated from the transmission spectrum using equation 2.24.

4.1 Simulation Procedures

Simulations of the porous optical waveguide were performed using the Ansys Lumerical MODE solver. The aim of the simulations is two fold; investigating the confinement factor as a function of porosity of mesoporous waveguides in air and water, and studying the difference in confinement factor of the mesoporous waveguide in water, ethanol and methanol. Following in this section is first the procedure for defining the simulation object in Ansys Lumerical and a description of the modal analysis performed. Then the procedure for confinement factor measurements and an overview of the measurements performed to investigate the relation to porosity is included. Finally, the procedure of simulating confinement factor in the mesoporus optical waveguide with solutions is described.

4.1.1 Defining Simulation Object and Performing Modal Analysis

Before performing modal analysis and confinement factor calculation, the simulation object was defined. The following description draws on previous accounts of work with Ansys Lumerical in the specialization project in January 2023. The Ansys Lumerical MDOE solver is as mentioned a recognized tool for waveguide simulations. The software has an extensive materials

list, but to ensure control of the characteristics of the materials the list was augmented with specific, customized materials; Silicon, Silicon Dioxide and Titanium Dioxide. Figure 4.1 shows the the geometries of the cross section of the mesoporous optical waveguide simulated and later fabricated. The bottom layer is Silicon (Si) with refractive index $n_{Si} = 4$ [32], the second layer and bottom cladding is Silicon Dioxide (SiO_2) with refractive index $n_{SiO_2} = 1.45$ [33] and the waveguide core is made of simulated mesoporous Titanium Dioxide (TiO_2) with the non-porous inherent refractive index of $n_{TiO_2} = 2.2813$ [34]. The program does not have settings to change porosity of materials, so in order to simulate a porous optical waveguide, the refractive index of the core is adjusted to mimic a change in porosity following Bruggeman's model in eq. 2.72. The thickness of the TiO_2 layer is h, the height of rib is s and the width of the rib waveguide is w.

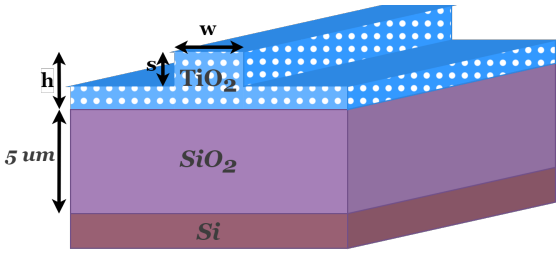

Figure 4.1: Cross section of a porous waveguide and its geometric variables. Thickness of TiO_2 layer $= h$, height of rib $= s$, width of waveguide $= w$.

The waveguide is positioned to be centered around $(0, 0, 0)$ in the program, meaning the propagation direction is z, the width of the waveguide is in the x-direction and the height in the y-direction. To define the simulation object, the rectangles of the defined materials were created in the software. To simulate the rib and slab of TiO_2, four rectangles were used. One for the left slab, one for the rib in the middle, one as a constant $50nm$ tall buffer with the same width as the rib, and one for the right slab. This was to ensure more freedom when simulating different thicknesses of the core and rib heights. The specifications of the height and width of these rectangles were adjusted according to the simulation needs, but the range of the outer slabs and the length of the waveguide remained constant. The length and total width of the waveguide are not as important during simulations, as the program uses cross-sectional measurements and the main interest of the simulations is the field distributed close to the rib. Thus, the total length in z-direction was set to be very small at $l = 1000nm$ and the total width in x-direction to be large enough at $w_{total} = 50000nm$ for it to not interfere with the field in the rib. The thicknesses of the rectangles for the SiO_2 and Si layers were both set to the constant height of $h_{Si/SiO_2} = 5000nm$ with the same total width and length as the core.

After defining the object, the external material around the waveguide was defined by inserting its refractive index. In simulations for this thesis the external materials were alternated between air, water, ethanol and methanol with the respective refractive indices; $n_{air} = 1$, $n_{water} = 1.32$ [30], $n_{ethanol} = 1.35$ [31], $n_{methanol} = 1.31$ [31]. The simulation temperature was set to $300K$. Subsequently, the finite difference eigenmode (FDE) solver was defined. Its center was defined to be the same as for the waveguide, and it was made to span across the waveguide, but not wider or lower than the Si substrate. Also it was sufficiently tall above the waveguide to account for field leakage to the air. The sizing for the FDE was as follows; $x_{min} = -22500nm$, $x_{max} = 22500nm$, $y_{min} = -7500nm$ and $y_{max} = 2500nm$. Furthermore, the boundary conditions for all sides of the FDE were set to be perfectly matched layers (PMLs).

Continuing, a fine mesh around the rib of the waveguide was defined to allow for finer

calculation here. This is where the field is expected to propagate and have its center of confinement, hence, where the results of the field calculation is the most interesting. The mesh was optimized using convergence testing, resulting in a mesh size of $x_{mesh} = 7100nm$, $y_{mesh} = 4000nm$, step size $t_{mesh} = 10nm$.

For modal analysis, the simulation object was defined and then modal analysis settings were defined. These include the wavelength at which the calculation is done, the number of trial modes tested, the range of refractive indices in which the modes are tested and the bending radius. Due to the nature of the fabricated waveguide being straight, the bending radius was set to zero for simulations in this thesis. The wavelength for the simulations was set to 1550nm as this is the typical wavelength of the NIR laser used for characterization [35]. The modal analysis was performed for 10 modes in the refractive index range of $n_1 = n_{maxTiO_2} = 2.2813 \rightarrow n_2 = n_{SiO_2} = 1.45$.

When the settings are selected and the specific geometries and refractive indices for the particular modal calculation set, the modal analysis is run and the modes are calculated. After running, the software presents a mode list with characteristics of the field in the specific modes. Furthermore, a mode plot showing how the field propagates through the waveguide is also presented. Figure 4.2 shows a mode plot from one of the simulations to illustrate.

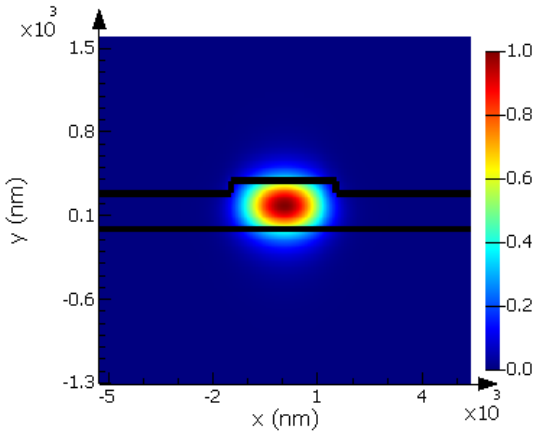

Figure 4.2: Example of mode plot from modal simulation retrieved from Ansys Lumerical.

After modal analysis, the script for calculation of confinement factor can be run as described in section 3.1.3.

4.1.2 Simulating Confinement Factor as a Function of Porosity

Earlier work such as [36] indicate that a mesoporous core waveguide design used for gas sensing can increase the light-matter interaction of the target media in the top cladding. The confinement factor of the target medium increases and the mesoporous waveguide sensor will be able to detect the medium with higher sensitivity since the light transmission in the waveguide will be more heavily affected by the target medium. As seen in section 2.2.4, the confinement factor is related to both the field distributions in a medium in a waveguide as well as the refractive index of the medium. The equation for confinement factor is repeated in eq. 4.1 for convenience. Here n_i is the refractive index of the medium and n_g is the group

refractive index in the medium.

$$\Gamma_i = \frac{n_g}{n_i} \frac{\iint_i \epsilon |\tilde{\boldsymbol{E}}|^2 dxdy}{\iint_{-\infty}^{\infty} \epsilon |\tilde{\boldsymbol{E}}|^2 dxdy} \tag{4.1}$$

Porosity, as defined by Bruggemanns model descibed in section 2.3, is in turn directly dependent on the refractive index of the porous medium. The model rearranged for porosity is repeated in equation eq. 4.2. Here n_{m1} is the refractive index of the medium where pores are present, n_{m2} is the refrative index of the medium inside the pores, and n_p is the refractive index of the porous medium.

$$p = \frac{(n_{m2} + 2n_p)(n_{m1} - n_p)}{3n_p(n_{m1} - n_{m2})} \tag{4.2}$$

Hence, the porosity of the waveguide also affects its ability to guide light as a too high porosity will decrease the confinement within the waveguide core when sensing gas. A balance in porosity and confinement factor must therefore be found. For liquid sensing using mesoporous optical waveguides, the effect of porosity on confinement factor might be different than in gas sensing. As a part of the exploration to use mesoporous optical waveguides for liquid sensing, the relation between porosity of the core of the waveguide and the confinement factor in the porous core is investigated by simulation. It will indicate whether high porosity contributes to high confinement in a mesoporous optical waveguide when used for liquid sensing. To do this, calculations of the relation between the porosity and the confinement factor of the target medium have been made for both air and water.

The Bruggemanns model rearranged for porosity and the confinement factor calculation script described in section 3.1.3 were used. Mode solver simulations were done in Ansys Lumerical with different core refractive indices to account for different porosities of the core. The mode simulations gave the different field contributions in the different media and were further used in the running of the confinement factor calculation script. However, as the software does not allow for porosity to be directly simulated, the porosity was simulated by changing the refractive index of the core material to account for a porous medium. To calculate the confinement factor of the media within the pores, the equation shown in eq. 4.3 was used. Γ_p is the confinement factor of the porous waveguide, Γ_{m1} is the confinement factor of the waveguide core and Γ_{m2} is the confinement factor of the material inside the pores. In the case of these simulations, the material inside the pores was presumed to be air with refractive index $n_{m2} = 1$ for one set of measurements, and water with refractive index $n_{water} = 1.32$. The waveguide core material was simulated to be TiO_2 with refractive index $n_{m1} = 2.2813$ [34].

$$\Gamma_p = \Gamma_{m1} \times p + \Gamma_{m2} \tag{4.3}$$

The geometry of the waveguide in these simulations plays a part, and for simplicity, the same geometry was used for every confinement factor calculation; $h = 400nm$, $s = 100nm$, $w = 3000nm$. The range of porosities tested was $25\% < p < 40\%$ and the different porosities chosen in relation to the refractive index of the porous core. The porosity range was chosen to reflect the porosities possible to fabricate using the Sol-gel method used for fabrication for this thesis.

Table 4.1 shows an overview of the characteristics used in simulations to explore the relation between porosity and confinement factor in mesoporous waveguides. n is the refractive index of the waveguide core inserted into Ansys Lumerical, n_{m1} is the inherent refractive index

of the TiO_2 in the core, n_{m2} is the refractive index of the material permeating the pores, in this case air or water, and p is the simulated porosity of the waveguide.

Table 4.1: Characteristics used in simulations to explore the relation between porosity and confinement factor in mesoporous waveguides. n is the refractive index of the waveguide core, n_{m1} is the inherent refractive index of the TiO_2 in the core, n_{m2} is the refractive index of the material permeating the pores, p is the simulated porosity of the waveguide.

	n	n_{m1}	n_{m2}	p
Waveguide in air	1.70	2.28	1	39.14%
	1.75	2.28	1	35.54%
	1.80	2.28	1	32.00%
	1.85	2.28	1	28.51%
	1.90	2.28	1	25.06%
Waveguide in water	1.87	2.28	1.32	39.14%
	1.90	2.28	1.32	35.53%
	1.94	2.28	1.32	32.01%
	1.97	2.28	1.32	28.51%
	2.01	2.28	1.32	25.09%

4.1.3 Simulating Confinement Factor in Mesoporous Optical Waveguides with Solutions

In addition to simulating the confinement factor in relation to porosity, the mesoporous optical waveguides' confinement in relation to the different solutions later to be disposed onto the waveguide was simulated. This was done to see the expected confinement in the mesoporous waveguides when adding different solutions. The geometry of the simulation object was the geometry of the waveguide was made to mirror the geometry of the real fabricated waveguide used in characterization and transmission experiments. Furthermore the porosity used to calculate the corresponding refractive index of the porous core was $p = 38\%$, as measured by ellipsometry. The refractive indices are again calculated using the Bruggeman method in section 2.3. Table 4.2 shows an overview of the specifications of the simulated waveguide. n_{m1} is the refractive index of the non-porous TiO_2 at 1550nm retrieved from [34]. n_{water} is the refractive index of water at 1550nm [30] and $n_{ethanol}$ and $n_{methanol}$ are the refractive indices of ethanol and methanol at 1550 nm [31].

Table 4.2: Overview of the specifications of simulated mesoporous optical waveguide.

Specification	**Value**
h	440 nm
s	100 nm
w	2600 nm
p	38%
n_{m1}	2.2813
n_{water}	1.32
$n_{ethanol}$	1.35
$n_{methanol}$	1.31

The same procedure for modal analysis and confinement calculation as above was followed

for these simulations. Firstly, the specifications for the materials were set, then modal analysis was performed and finally the confinement factor was calculated using the script described in section 3.1.3.

4.2 Fabrication Procedures

The mesoporous optical waveguide was fabricated using the Sol-gel method outlined in section 3.2.1. Section 4.2.1 describes the procedure followed using the Sol-gel method and the specifications of the finifshed mesoporous optical waveguide. In addition, a microfluidic cell was fabricated using PDMS to contain liquid onto the waveguide sample during measurements. The procedure following the method for PDMS fabrication described in section 3.2.2, is described in section 4.2.2.

4.2.1 Fabrication of Mesoporous Optical Waveguides

The fabrication of the mesoporous optical waveguide is done using a prefabricated Silicon Dioxide (SiO_2) on Silicon (Si) 4" wafer. The layer of SiO_2 is 5μm thick and the thin film on top is made of TiO_2 due to TiO_2's refractive index and conductivity. The theoretical refractive indices of the layers of the waveguide are; $n_{Si} = 3.5$ [32], $n_{SiO_2} = 1.47$ [33], $n_{TiO_2} = 2.03$ [34].

The mesoporous TiO_2 layer is deposited onto the wafer using the Sol-gel method as described in section 3.2.1. Briefly summarized, a solution of Titanium Chloride ($TiCl_4$) and ethanol (C_2H_6O) is mixed with an aqueous solution of pluronic F127 to avoid bonding between the $TiCl_4$ and the polymers. The new solution is spin-coated onto the prefabricated $Si-SiO_2$ wafer and heated step-wise up to 350°C. The reaction gives the following chemical equation 4.4 where TiO_2 is solid crystal and HCl is gaseous.

$$TiCl_4 + 2H_2O = TiO_2(s) + 4HCl(g) \tag{4.4}$$

The gaseous HCl evaporates and the polymers from the pluronic F127 are combusted due to the heating. Hence, left on the wafer is solid TiO_2 with pores created by the combusted polymers. The pores naturally form a continuous and even pattern in the TiO_2. Figure 4.3 shows an illustration of the layers on the wafer.

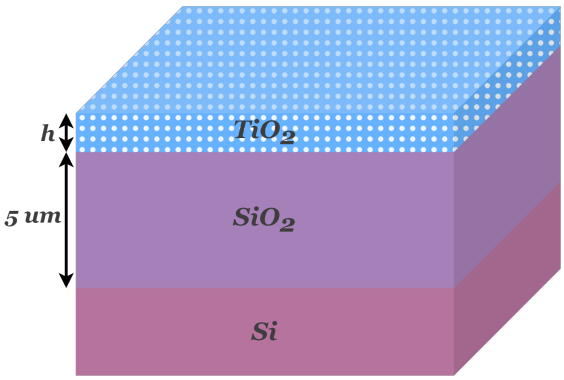

Figure 4.3: Illustration of layers on wafer after using Sol-Gel method to deposit mesoporous TiO_2 onto $Si-SiO_2$ wafer. h is the thickness of the mesoporous layer.

In order to get a thicker layer of mesoporous TiO_2, the process of fabricating the layer can be repeated to result in a double layer, however this might offset the pore-pattern and cause inhomogeneity. After depositing the mesoporous TiO_2 layer onto the wafer, lithography is used for patterning. The pattern of the waveguides is etched using a mask designed by Jana Jágerska and Sebastian Alberti, shown in appendix B. A close-up of the mask used is shown in figure 4.4.

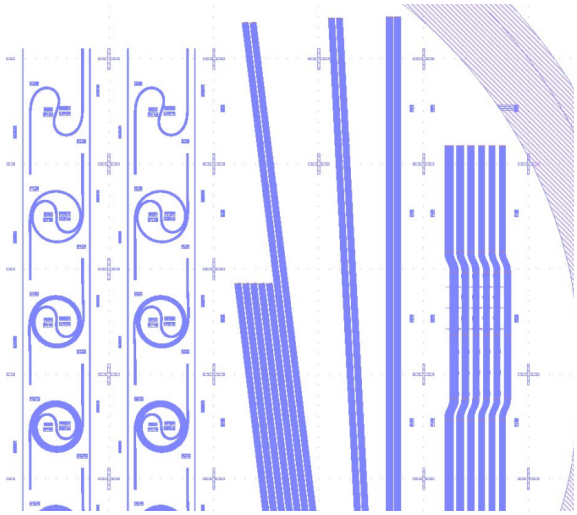

Figure 4.4: Close-up of of etching mask used in fabrication of mesoporous optical waveguides of different length and size. See appendix B for full mask.

The mask used has rib waveguides with different length and shape; both straight, bent and spiral rib-waveguides. This is to be able to test different types of losses and propagation through the mesoporous waveguide. In order to use the waveguide in sensing applications, the goal is a mesoporous waveguide spiral, as it can have long propagation distance on a small area. The bending radius of the spirals shown in the mask is $r_{bending} = 1.05 \times 10^{-6} m$. After etching, the wafer is cut into chips with different waveguides using the cut lines visible in the mask. The cross section previously shown in figure 4.1 is a good visual representation of the cross section of the finished fabricated mesoporous waveguide.

4.2.2 Fabrication of Microfluidic Cell

In order to establish consistent, uniform distribution of solutions onto the waveguide sample, as well as to prevent evaporation during ongoing experiments, a microfluidic cell was constructed and positioned atop the sample and waveguide. A pipette was used to fill the cell with solution throughout experiments and a lid placed over the cell to prevent evaporation. The microfluidic cell was fabricated using polydimethylsiloxane (PDMS) due to its previous utilization in microfluidic research [22]. By using the PDMS cell, the aim is to ensure repeatability and maintain the integrity of the experimental conditions throughout the measurements.

Following the method explained in section 3.2.2, the PDMS solution was deposited into a two inch Petri dish with a thickness of five millimeters. The solution was heated to 65° for four hours to cure. After curing, the hardened PDMS was cut into appropriate cell and lid sizes for the sample sizes using a scalpel and circular puncher with a diameter of six millimeters. Figure 4.5 shows an illustration of the construction of the microfluidic cell and its placement on a sample.

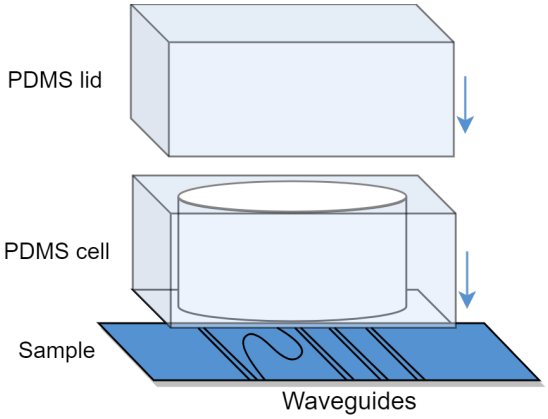

Figure 4.5: Microfluidic cell to keep solutions dispensed onto sample and waveguide during characterization experiments. Fabricated using cut PDMS of 5mm height. Cell hole size is 6mm in diameter.

The total width of the microfluidic cell was fabricated to allow for a 2 mm lip of protruding sample on either side. This was done to allow for coupling in and out of the waveguide on the sample using a microscope, as the waveguides on the sample are not visible through the PDMS cell. The cell fabricated to contain dispensed solution was 6mm in diameter and circular, spanning over the waveguides on the sample.

4.3 Characterization Procedures

In order to investigate the behaviour of the mesoporous optical waveguides when exposed to liquid solutions, characterization using ellipsometry and NIR transmission measurements were performed. The aim of the ellipsometry measurements is to characterize the waveguide's core thickness, refractive index and porosity, while the aim of the transmission measurements using a NIR tunable laser setup is to measure the transmission spectrum of the mesoporous waveguide with different solutions as top cladding. The absorption spectrum was thus calculated from the transmission spectrum using equation 2.24. Section 4.3.1 contains the procedure followed for ellipsometry measurements, while section 4.3.2 presents the procedure for the transmission measurements.

4.3.1 Ellipsometry

The thickness of the the TiO_2 layer h, the refractive index n and the porosity p of the mesoporous optical rib waveguide was measured using ellipsometry. Ellipsometry is methodically explained in section 3.3.1. Following in this section is an introduction to the ellipsometer used, a section on the method for measurements of thickness and refractive index, and a section on the method for measurement of porosity.

The *Semilab SE-2000 Spectroscopic Ellipsometer* was chosen due to its wide spectral range, thin film field of application and ability to measure porosity. More detailed information about the apparatus can be found on Semilab's web-page [37]. Figure 4.6 shows a labelled image of the ellipsometer.

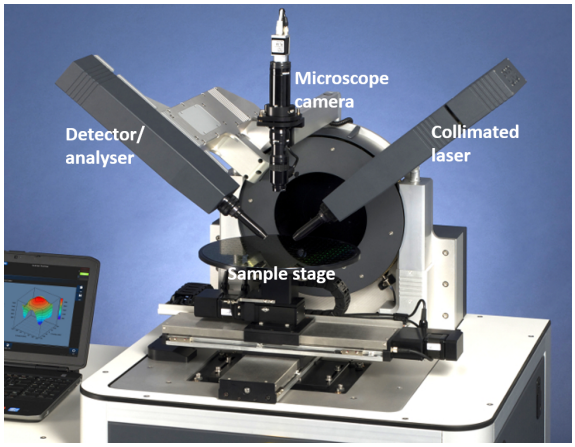

Figure 4.6: Semilab SE-2000 Spectroscopic Ellipsometer with labels. Adapted with labels from [37].

When beginning a measurement, the sample should be positioned on the sample stage between the laser and detector. Through the use of the microscope camera, the desired area of the sample can be aligned with the laser's point of reflection. To ensure accurate measurements, the stage can be adjusted along the x, y, and z axes using the ellipsometer's software. Figure 4.7 shows an image from the microscope camera when imaging a spiral waveguide.

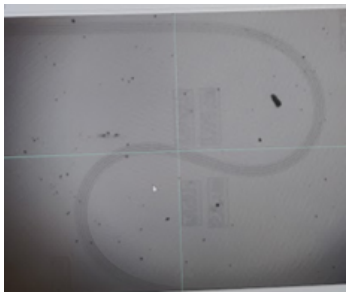

Figure 4.7: View of spiral waveguide from microscope camera.

After placing the area of interest of the sample on the stage, the ellipsometer is focused using the software. When the focus of the laser is in the chosen focus area, the measurements can begin. The measurement of thickness and refractive index is done simultaneously and follows the theory described in section 3.3.1. The measurement of porosity is done separately by placing the sample in a humidity chamber.

To measure the thickness and refractive index of the sample, it was first placed on the stage, focused in one point, and later moved using the software's adjustment settings without changing the focusing settings. After focusing on the first measurement point, a measurement was made by starting the software. As stated in the theoretical background, the measurement gives an output of graphs of $\tan\Psi$ versus wavelength λ and $\cos\Delta$ versus wavelength. These graphs are then used in a best-fit calculation using a dispersion model. As all the samples measured for this thesis are TiO_2 thin films, thus the same dispersion model was used for all. Several models for oxides were tested and the model with the best results was the Forohui-Bloomer dispersion model. The reference [38] gives more detailed descriptions of this dispersion model. Finding the best-fit to the model for all measurements on the sample, required some adjustment of the different constants in the dispersion model. After finding the model of best-fit, the thickness and refractive index are calculated from the model and also shown in the software.

For porosity measurements, the sample is placed in the humidity chamber of the setup, and the humidity is changed stepwise with default settings. Measurements are automatically done after every step, giving a graph of change in refractive index and layer thickness due to humidity. The change in layer thickness is negligible as the change in humidity has little effect on this. The refractive index graph is presented in the software as refractive index versus relative pressure in the chamber and shows both absorption and desporption. The pores of the mesoporous optical waveguide fill with water vapour, depending on the humidity percentage in the chamber, ultimately changing the refractive index of the sample. The change in refractive index is measured and the porosity is calculated using the Bruggeman effective medium approximation outlined in section 3.3.1. The final measured porosity is presented in the software.

4.3.2 NIR Transmission Measurements

Characterization of the mesoporous optical waveguide to investigate the effects of dispensed liquids, was also done using transmission measurements with a tunable near infrared laser. Firstly, the sample was prepared with the microfluidic PDMS cell and lid and aligned. Measurements were done using multiple solutions of water, ethanol and methanol.

The laboratory setup is shown in figure 4.8. A detailed list of components used in this setup is found in table 4.3.

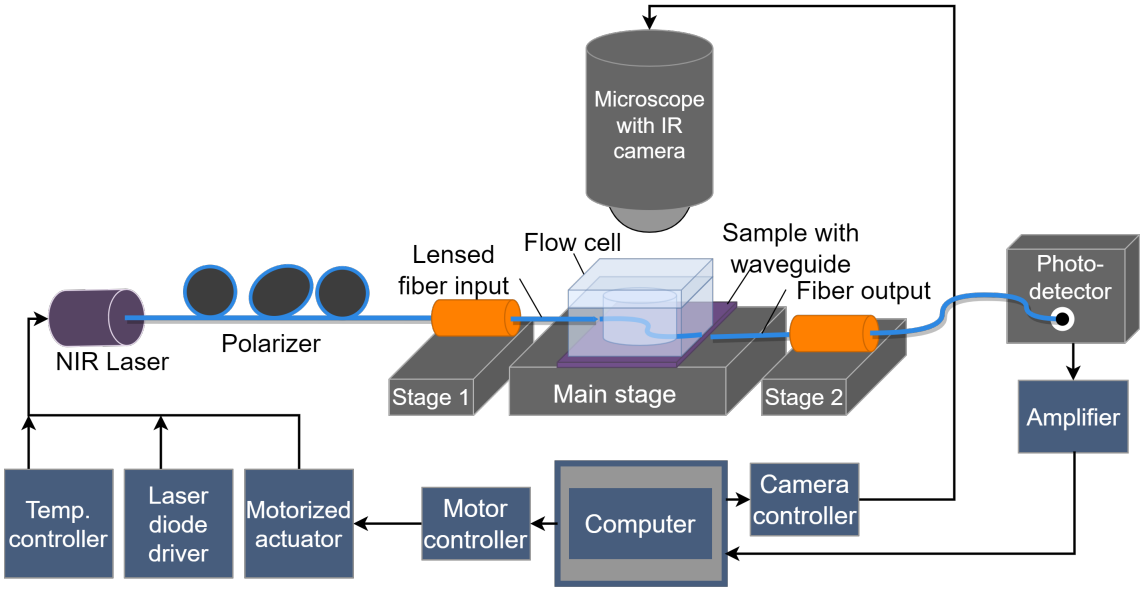

Figure 4.8: Laboratory setup for transmission measurements using NIR tunable laser TLK-L1550M.

Table 4.3: Overview of components in laboratory setup used in characterization of waveguides. A visual representation of the transmission measurement setup and the components' connection is shown in figure 4.8.

Component	Model	Manufacturer
Near Infrared Tunable Laser	TLK-L1550M	Thorlabs
Laser diode driver	Newport	505
Motorized actuator	Z812	Thorlabs
Motor controller	TDC001	Thorlabs
Temperature controller	325	Newport
Lensed fiber	TSMJ-X-1550-9/125-0.25-7-2.5-14-2	OZ Optics
Polarizer	FPC560	Thorlabs
Microscope		Leitz Wetzlar
Camera		Hamamatsu
Camera controller	C2400	Hamamatsu
Optical fibers	SMF-28 Ultra	Corning
Photodetector	DET10C2	Thorlabs
Amplifier	PDA200C	Thorlabs

The TLK-L1550M NIR tunable laser with tuning range of 1460nm-1640nm is driven by a Newport 505 laser diode driver and a piezoelectric motor controlled by a TDC001 motor controller and Z812 actuator managed by software on a computer. The manual for the tunable laser can be found in [35]. Furthermore, the laser is connected to a 325 Newport temperature controller. The laser output is coupled into a fiber that is polarized with an FPC560 polarizer. The TSMJ-X-1550-9/125-0.25-7-2.5-14-2 input fiber has a lensed output mounted on stage 1 which allows translation in x, y and z directions using screws. Above the main stage where the sample is placed, a microscope with an infrared camera is mounted. The camera is controlled

by a Hamamatsu C2400 camera controller that is in turn managed by software on a computer. The output of the waveguide on the sample is collected by a SMF-28 Ultra multimode fiber output mounted on stage 2. Stage 2 is also an x, y and z translation stage. The multimode fiber is connected to a Thorlabs DET10C2 detector that is amplified through a Thorlabs PDA200C amplifier and connected to the computer.

The sample was placed on the main stage shown in figure 4.8 and aligned manually to have the waveguide parallel to the stage. The microscope was positioned above the output of the waveguide to help with further alignment. The receiving multi mode fiber was moved close to the sample and the waveguide by moving Stage 2 in the x direction so that the exposed end of the waveguide is aligned with the end of the fiber. Subsequently, the microscope was moved to the opposite side of the sample and the lensed input fiber was brought close to the waveguide and adjusted roughly. The laser was turned on and the infrared camera was adjusted to give a good view of the input fiber and the waveguide input. The laser output power was then turned down to 100mA to ensure that the camera doesn't saturate. Furthermore, the input fiber was adjusted to account for a highly efficient edge coupling as seen in [39]. After visually coupling using the IR camera, the power of the laser was turned up to 399.6 mA and the wavelength set to 1550 nm in the software lab program Labview [40]. The input and output fibers were then finely tuned in the x, y and z direction to achieve the most efficient coupling. After maximizing the output intensity at the receiver, five sweeps of the waveguide range 1460 nm - 1640 nm were done in succession and mean averaged. Lastly, the fibers were removed from the sample and the sample removed from the stage to prepare it for the next set of measurements.

Nine different solutions of ethanol and water or ethanol and methanol were used in transmission measurements. The solutions are listed in table 4.4. Furthermore, two different control measurements were performed on the waveguide. These are listed in table 4.5. Measurements using the different solutions and control measurements were made in three different sequences. These sequences are shown in table 4.6. Overall, 5 repetitions per measurement set in every sequence were performed using the laboratory setup explained above. Finally, control measurement B was performed separately.

Table 4.4: Solutions of ethanol, water and methanol used in transmission measurements of mesoporous optical waveguides.

	Ethanol (%)	**Water (%)**	**Methanol (%)**
Solution A	0	100	0
Solution B	25	75	0
Solution C	50	50	0
Solution D	75	25	0
Solution E	100	0	0
Solution F	0	0	100
Solution G	25	0	75
Solution H	50	0	50
Solution I	75	0	25

Table 4.5: Overview of control measurements used for transmission measurements of mesoporous optical waveguides.

	Conditions
Control measurement A	Sample with PDMS cell with air
Control measurement B	Background measurement of optical fiber to fiber in air

Table 4.6: Sequences of measurements made on mesoporous optical waveguide. In addition, control measurement B was performed separately.

Sequence 1:	***Sequence 2:***	***Sequence 3:***
Control A	Control A	Control A
Solution A	Solution A	Solution F
Solution B	Solution B	Solution G
Solution C	Solution C	Solution H
Solution D	Solution D	Solution I
Solution E	Solution E	

To dispense solutions into the microfluidic cells on the samples, a simple procedure was repeated for all measurement sets. The procedure is shown visually in figure 4.9. After attaching the PDMS microfluidic cell and lid to the sample, the lid was removed using tweezers. Furthermore, the solution was dispensed in droplets into the open cell using a pipette, making sure the meniscus of the solution did not extend past the cell walls. The lid was then replaced atop using tweezers with gentle pressure to ensure the microfluidc cell was sealed. The sample with the filled microfluidic cell could then be aligned under the microscope again.

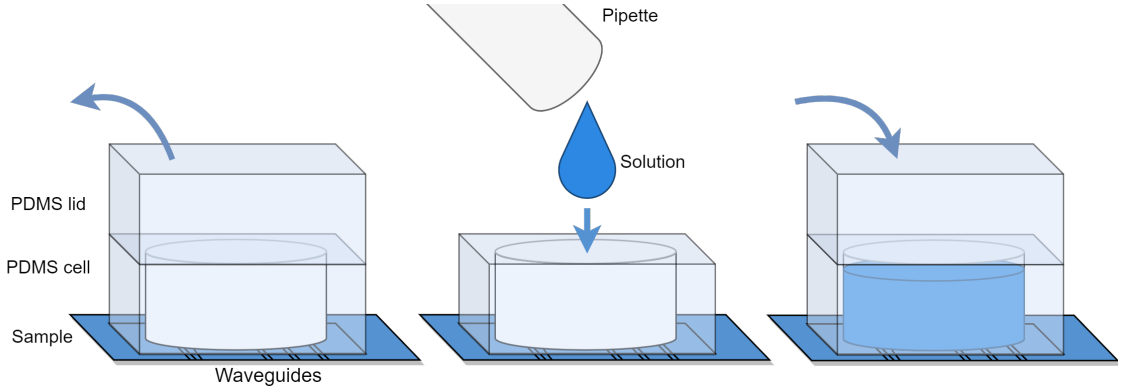

Figure 4.9: Illustration of the procedure used for dispensing solutions into the microfluidic cell and onto the samples. The PDMS lid is removed using tweezers, droplets of solution are added using a pipette and the lid is replaced applying pressure to achieve a seal.

After measuring a solution, the sample was removed from the stage, the lid was removed and the sample placed on a hot plate. The sample with the PDMS cell still attached, was heated to 65°C for 5-10 minutes to let the previous solution evaporate from the sample surface and the pores. It was then cooled down and a new solution was added in the same manner as described above.

4.3.3 Signal processing

The data is collected as amplitude versus wavelength between $1460nm - 1640nm$. Due to the piezoelectric motor driving the laser at a set speed across the wavelength range, the raw data consists of an irregular number of data points in the wavelength range. After retrieving the raw data, signal processing was therefore required to analyse it and compare different results. Signal processing and plotting of data was done using MatLab. The procedure of signal processing performed on every measurement was the following:

1. ***Limiting of data between wavelengths*** $1460nm < \lambda < 1600nm$***:*** To have a smaller analysis range and remove excess data points on the edge of the wavelength range, limiting was performed by indexing the wavelength data.
2. ***Interpolation of data giving 560 data points to every measurement:*** To correct for the uneven number of data points, the data is interpolated. Different interpolation methods were tested to ensure minimal alterations to the measured spectra, and the spline interpolation method gave preferable results. The MatLab function *interp1* was used to perform the interpolation.
3. ***Filtering using Savitzky-Golay filtering:*** To smooth out fringes received due to Fabry-Perot interference, Savitzky-Golay filtering as described in section 3.3.2 was performed using the MatLab function *sgolayfilt*.
4. ***Removal of background measurement by division***: The background was measured in a separate control measurement B. It was removed from other measurements through division.

Chapter 5

Results and Discussion

This chapter separately presents and discusses results from the simulation, fabrication and characterization performed to investigate the possibility for liquid sensing in mesoporous optical waveguides. Firstly, in section 5.1 the results from simulations in Ansys Lumerical MODE solver will be discussed and analysed. Next, the results from fabrication of the mesoporous waveguide and the microfluidic PDMS cell will be discussed in section 5.2. Following, results from the characterization techniques using ellipsometry and transmission measurements will be presented and discussed in section 5.3. Finally, a summarizing discussion is included in section 5.4.

5.1 Simulations

The simulations were performed using Ansys Lumerical MODE Solver as described in section 4.1. Firstly, the simulation object was defined with desired geometry and material compositions. Secondly, simulations were performed to inspect and analyse confinement factor as a function of porosity using a general structure size with air and water as top cladding. Finally, confinement factor in the mesoporous optical waveguides with solutions disposed on top, was simulated to observe the effect of the different solutions water, ethanol and methanol as top cladding and present in the pores.

5.1.1 Confinement Factor as a Function of Porosity

The simulations of confinement factor to analyse its relation to porosity were done using the geometry; $h = 400nm$, $s = 100nm$, $w = 3000nm$, where h is the thickness of the mesoporous layer, s is the rib height of the rib waveguide, and w is the width of the rib. The range of porosities p tested, was $25-40\%$ as this range is possible to fabricate using the Sol-gel method described in section 3.2.1. The refractive indices are calculated using the Bruggeman method in section 2.3 and n is the refractive index of the simulated mesoporous waveguide, n_{m1} is the refractive index of the non-porous TiO_2 at 1550nm retrieved from [34], while n_{m2} is the refractive index of the simulated contents of the pores. Simulations to see the relation between porosity and confinement factor were made with the mesoporous waveguide in air and in water. The different measurement conditions and the corresponding simulated confinement factors in air are shown in table 5.1. Figure 5.2 shows a graphical representation of the relation between porosity and simulated confinement factor in air.

Table 5.1: Simulated confinement factors in relation to simulated porosities of mesoporous optical waveguides in air in Ansys Lumerical MODE solver using the geometries; $h = 400nm$, $s = 100nm$, $w = 3000nm$.

n	n_{m1}	n_{m2}	p	Γ_n	Γ_{m2}	Γ_p
1.70	2.28	1	39.14%	50.67%	3.77%	23.61%
1.75	2.28	1	35.54%	62.35%	4.40%	26.56%
1.80	2.28	1	32.00%	69.95%	4.62%	27.01%
1.85	2.28	1	28.51%	75.56%	4.65%	26.19%
1.90	2.28	1	25.06%	79.89%	4.56%	24.58%

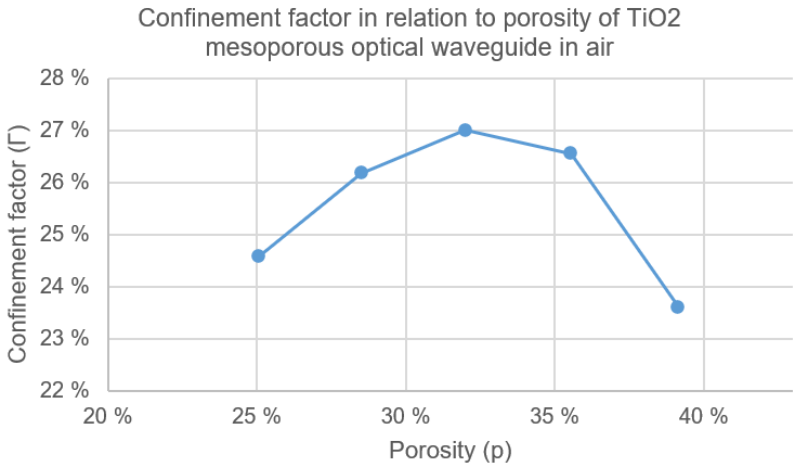

Figure 5.1: Graphical presentation of simulated confinement factors in air in relation to simulated porosities of mesoporous optical waveguides in Ansys Lumerical MODE solver using the geometries; $h = 400nm$, $s = 100nm$, $w = 3000nm$.

From these results it is evident that the highest confinement factor in a mesoporous optical waveguide with a porous TiO_2 core in air, with the geometries mentioned above, are found with a porosity between $30-35\%$. This porosity is achieved in simulation by using a refractive index of the porous core material as between approximately $1.75-1.83$ following the Bruggeman model in equation 2.72. This peak in confinement factor around this porosity range indicates that there is a limit of porosity for a mesoporous optical waveguide to guide well in air. The field in a highly mesoporous waveguide with pores filled with air, is likely leaking more into the cladding and substrate of the waveguide, giving low confinement in the air in the pores and above the waveguide.

Table 5.2 shows the different measurement conditions and the corresponding simulated confinement factors in water. Figure 5.2 shows the data represented in a graph.

Table 5.2: Simulated confinement factors in relation to simulated porosities of mesoporous optical waveguides in water in Ansys Lumerical MODE solver using the geometries; $h = 400nm$, $s = 100nm$, $w = 3000nm$.

n	n_{m1}	n_{m2}	p	Γ_n	Γ_{m2}	Γ_p
1.87	2.28	1.32	39.14 %	75.02 %	10.19 %	39.55 %
1.90	2.28	1.32	35.53 %	77.68 %	9.65 %	37.25 %
1.94	2.28	1.32	32.01 %	80.04 %	9.12 %	34.74 %
1.97	2.28	1.32	28.51 %	82.13 %	8.60 %	32.01 %
2.01	2.28	1.32	25.09 %	84.01 %	8.10 %	29.17 %

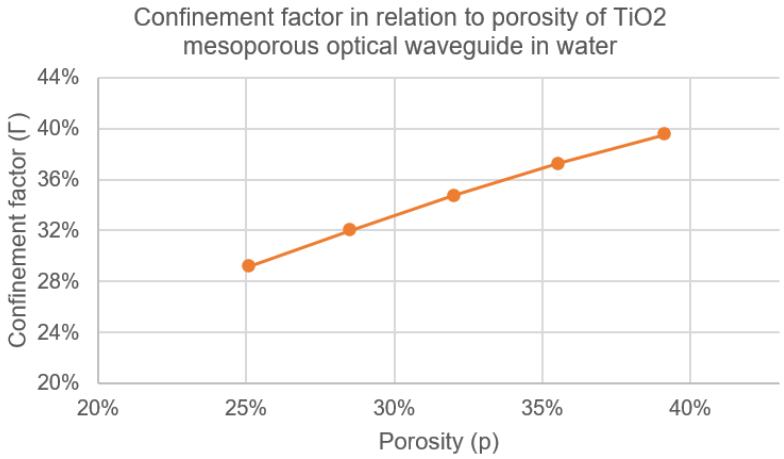

Figure 5.2: Graphical presentation of simulated confinement factors in water in relation to simulated porosities of mesoporous optical waveguides in Ansys Lumerical MODE solver using the geometries; $h = 400nm$, $s = 100nm$, $w = 3000nm$.

In contrast to the simulations in air, the confinement factor of the mesoporous waveguide in water does not have a peak in relation to the porosity of the core in the range tested. Rather, the graph shows that the higher porosity within this range, the higher the confinement factor in the waveguide. Hence, with more water penetrated into the waveguide due to a higher porosity, the light-matter interaction of the water increases. One could conclude that for liquid sensing, a highly porous waveguide core is preferable. This is further discussed below.

5.1.2 Confinement Factor with Different Solutions on Mesoprous Waveguide

When simulating confinement factor in the mesoporous waveguide in relation to the solutions water, ethanol and water, the geometry of the waveguide was made to mirror the geometry of the real fabricated waveguide used in characterization and transmission experiments. The thickness was $h = 440nm$, the rib height was $s = 100nm$ and the rib width was $w = 2600nm$. The confinement factor was calculated assuming a porosity of $p = 38\%$ which was the measured porosity of the waveguide using ellipsometry. The aim of the simulations was to see the expected confinement in the waveguide when adding the solutions later used in transmission measurements; water, ethanol and methanol. Results from the calculations are shown in table 5.3. The refractive indices are again calculated using the Bruggeman method in section 2.3. n is the refractive index of the simulated mesoporous waveguide and n_{m1} is the refractive index of the non-porous TiO_2 at 1550nm retrieved from [34]. n_{m2} is the refractive index at 1550nm

of the solutions diffusing into the pores and were retrieved from [30] for water and [31] for ethanol and methanol.

Table 5.3: Confinement factor in mesoporous optical waveguide with air and solutions water, ethanol and methanol.

Solution	n	n_{m1}	n_{m2}	p	Γ_n	Γ_{m2}	Γ_p
Air	1.72	2.28	1	38.0%	63.05 %	3.96 %	27.92 %
Water	1.88	2.28	1.32	38.0%	80.04 %	8.77 %	39.18 %
Ethanol	1.89	2.28	1.35	38.0%	80.22 %	9.38 %	39.87 %
Methanol	1.87	2.28	1.31	38.0%	79.49 %	8.67 %	38.87 %

Firstly, the results show that the confinement factor of the liquid solutions in the pores is much higher than with air, showing a stronger light-matter interaction when using liquid. This indicates that the mesoporous waveguide is favourable for liquid sensing. Moreover, the confinement factor of the porous waveguide in water is 0.69% lower than the confinement in ethanol, but 0.31% higher than in methanol. This can be explained by the refractive indices of the solutions, as confinement factor is directly related to the refractive index of the inspected medium as well as the field distribution. With a higher refractive index in the core compared to in the cladding, the light will more easily propagate and be more confined. Water has a refractive index of $n_{water} = 1.32$ which is 0.03 lower than $n_{ethanol} = 1.35$ and 0.01 higher than $n_{methanol} = 1.31$.

Furthermore, the higher confinement factor in the pores, the more light-matter interaction is occurring and the more the waveguide transmission is affected by the solution. Hence, the waveguide in ethanol should experience a more prominent effect in transmission than the waveguide in water or in methanol in transmission measurements. By rearranging the equation for intensity in relation to confinement factor in eq. 2.58 from section 2.2.4, we can calculate the expected transmission in the mesoporous optical waveguide in relation to the simulated confinement factor. Equation 5.1 shows the direct relation between transmission T and confinement factor Γ, where α is the absorption coefficient and L is the propagation length of the waveguide.

$$T = e^{-\alpha \Gamma L} \tag{5.1}$$

Table 5.4 shows the calculated transmission in the waveguide at the wavelength of $\lambda = 1550nm$, as a function of the confinement in the porous waveguide core Γ_n and as a function of the confinement in the solution permeating the pores Γ_p. The absorption coefficients for the solutions at this wavelength are retrieved from the absorption spectra in figure 3.4 and the length of the waveguide is the measured length shown in section 5.2.

Table 5.4: Calculated transmission at wavelength $\lambda = 1550nm$ as a function of confinement factors Γ_n and Γ_p using absorption coefficients from figure 3.4.

Solution	Γ_n (%)	Γ_p (%)	$1 - T_n$ (a.u.)	$1 - T_p$ (a.u.)
Water	80.04 %	39.18 %	1.07×10^{-8}	5.21×10^{-9}
Ethanol	80.22 %	39.87 %	5.74×10^{-9}	2.86×10^{-9}
Methanol	79.49 %	38.87 %	8.45×10^{-9}	4.13×10^{-9}

The results from table 5.4 show that the transmission T_n in the mesoporous waveguide with water as the top cladding and permeated into the pores is lower than both ethanol and

methanol. Ethanol also has higher transmission than methanol at 1550nm. The transmission in the pores of the mesoporous waveguide T_p follows the same pattern, where ethanol has the highest transmission and water the lowest due to the stronger absorption of water at this wavelength.

5.2 Fabrication

The mesoporous optical waveguide was fabricated and cleaved into 1x1 cm chips to fit into the laboratory setup described in section 4.3.2. The most suitable chip was chosen and the PDMS microfluidic cell was stuck onto the sample as described in section 4.2.2. Figure 5.3 shows the sample with the attached microfluidic cell placed on the main stage the laboratory setup for transmission measurements.

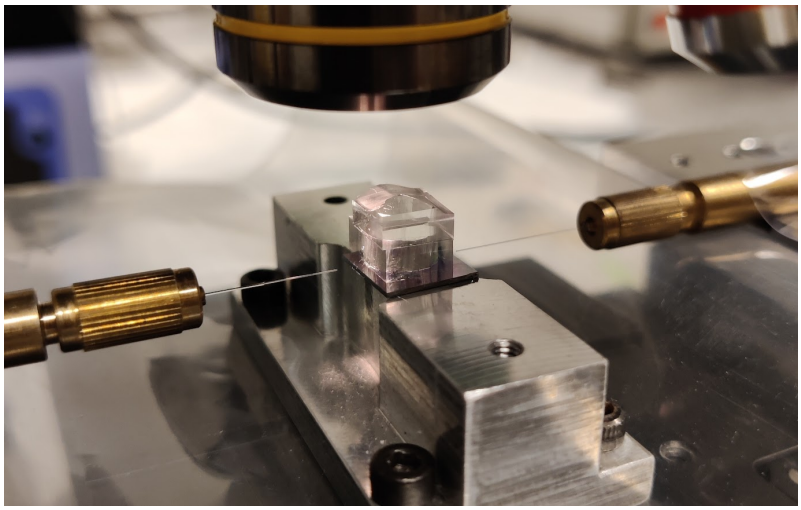

Figure 5.3: Sample of mesoporous optical waveguide in laboratory setup for transmission measurements with PDMS microfluidic cell attached.

The waveguide on the chip has the following geometry, where measurement L was made using a caliper and w, h and s found from information in the mask design of the waveguide.

- Length $L = 11mm$
- Width $w = 2600nm$
- Thickness of waveguide core $h = 440nm$
- Rib height $s = 100nm$

The PDMS microfluidic cell has the following geometry. Measurements were made using a caliper.

- Width across wavelength $w_{pdms} = 9mm$
- Diameter of cell for solution $d_{cell} = 6mm$
- Height of cell $h_{cell} = 4mm$
- Total height with lid $h_{tot} = 8mm$

5.2.1 Challenges in fabrication of mesoporous waveguide

Some issues encountered with the fabrication process have been noticed. One finding is that the pores made using the Sol-gel method seem to be partially filled with the photoresist polymer used when lithography patterning the waveguides. The problem is difficult to identify, but it presumably gives the waveguide different properties, for instance lower or no porosity. Some waveguides with this presumed issue were tested using ellipsometry and in the transmission measurement setup, but as results were unreliable, they are not included in this thesis. A solution to this problem has been tested by Alberti and is still in the making. It involves removing excess polymer by heat treatment and rinsing, and has had somewhat successful outcomes.

5.3 Characterization

Characterization of the mesoporous optical waveguide was done using ellipsometry and transmission measurements. The ellipsometry measurements revealed the thickness of the waveguide core, the waveguide's refractive index and its porosity. This data is used to perform simulations of the waveguide's confinement factor and transmission, as well as give more insight into the light propagation in the waveguide during the transmission measurements. The transmission measurements were performed following the procedure in 4.3.2 with the aim of investigating the effects of waveguide transmission when using solutions of water, ethanol and methanol as top cladding. The absorption spectrum was thus calculated from the transmission spectrum following equation 2.24.

5.3.1 Ellipsometry Measurements

The ellipsometry measurements resulted in the following data for the thickness of the waveguide core, the waveguide's refractive index and its porosity:

- $h = 439nm$ (thickness of waveguide core)
- $n = 1.89$ (refractive index of porous TiO_2 waveguide core)
- $p = 38\%$ (porosity of porous TiO_2 waveguide core)

5.3.2 NIR Transmission Measurements

The transmission measurements were performed in the laboratory setup in figure 4.8 on the straight mesoporous optical waveguide in figure 5.3 with the measured characteristics above. The three sequences of measurements outlined in section 4.3.2 are repeated below in table 5.5 for convenience.

Table 5.5: Sequences of measurements made on mesoporous optical waveguide. In addition, control measurement B was performed separately.

Sequence 1:	***Sequence 2:***	***Sequence 3:***
Control A	Control A	Control A
Solution A	Solution A	Solution F
Solution B	Solution B	Solution G
Solution C	Solution C	Solution H
Solution D	Solution D	Solution I
Solution E	Solution E	

Every solution or control measurement was performed with 5 sweeps. The raw data was limited between wavelengths 1460nm - 1600nm, interpolated using spline interpolation, filtered using Savitzky-Golay filtering, and finally the mean average of the five sweeps was calculated and the background removed by division of control measurement B. Due to the large amount of raw data collected, only the processed, mean data is presented in this thesis. Furthermore, to neglect the edge effects when processing, the data is presented in the range 1475nm-1585nm.

Sequence 1 consists of different concentrations of ethanol and water, as well as control measurement A without any solution. An overview of the solutions is found in table 4.4 but repeated here for convenience. Solution A contains pure water, Solution B contains 25% ethanol and 75% water, Solution C contains 50% ethanol and 50% water, Solution D contains 75% ethanol and 25% water, and Solution E contains 100% ethanol.

An expectation for this sequence of measurements is that the measurements made with solutions deposited onto the waveguide have higher transmission than the control measurement. This due to the refractive index of air ($n_{air} = 1$) being significantly lower than the refractive indices of the solutions ($n_{ethanol} = 1.35$, $n_{water} = 1.32$) and we expect higher leakage to the substrate and scattering loss with air as the top cladding and permeated into the pores.

Another hypothesis for the measurements is that the transmission spectra of the mesoporous optical waveguide will have higher peaks with higher concentrations of ethanol deposited as top cladding. This is explained by investigating the absorption spectra of water and ethanol, and the simulated confinement factor and transmission of the waveguide with water and ethanol as the top cladding at $\lambda = 1550nm$. The absorption spectra of ethanol and water outlined in section 3.3.3 indicate that water has four times higher absorption than ethanol in the range of the transmission measurements. As seen in table 3.1, the water spectrum has a peak of $\alpha_{water} = 2.8 \times 10^{-6}$ at 1450 nm, while the ethanol spectrum has a peak at 1581 nm of $\alpha_{ethanol} = 6.9 \times 10^{-7}$. The equation for transmission in relation to absorption coefficient outlined in section 2.1.2 and repeated in equation 5.2, confirms that a higher absorption coefficient α gives lower transmission T.

$$\alpha = -\frac{log(T)}{x} \tag{5.2}$$

Furthermore, in table 5.4 the confinement factor of the mesoporous waveguide in ethanol is 0.69% higher than the confinement factor of water, giving 2 times higher transmission T_n than in water at the wavelength of $\lambda = 1550nm$. This indicates that with the same porosity, deposition of a solution with ethanol onto the mesoporous waveguide allows for better transmission of the EM field than deposition of water. The lower confinement factor for water also indicates more loss through leakage to the substrate in the waveguide when using water than ethanol.

Figure 5.4 shows the results of measurements in *Sequence 1* while figure 5.5 is a plot of the maximum peaks to better visualize the difference between the solutions.

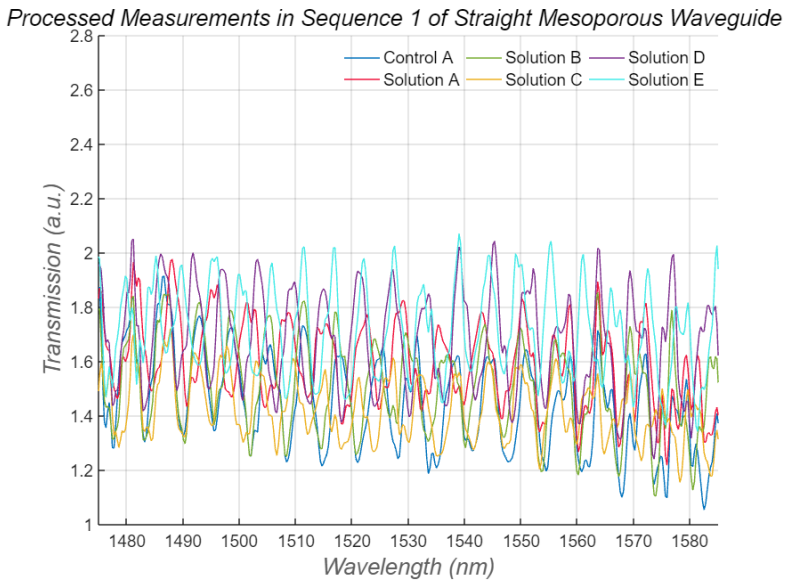

Figure 5.4: Processed measurements in Sequence 1; Control A in blue, Solution A in red, Solution B in green, Solution C in yellow, Solution D in purple, and Solution E in cyan. An overview of the solution compositions is found in table 4.4.

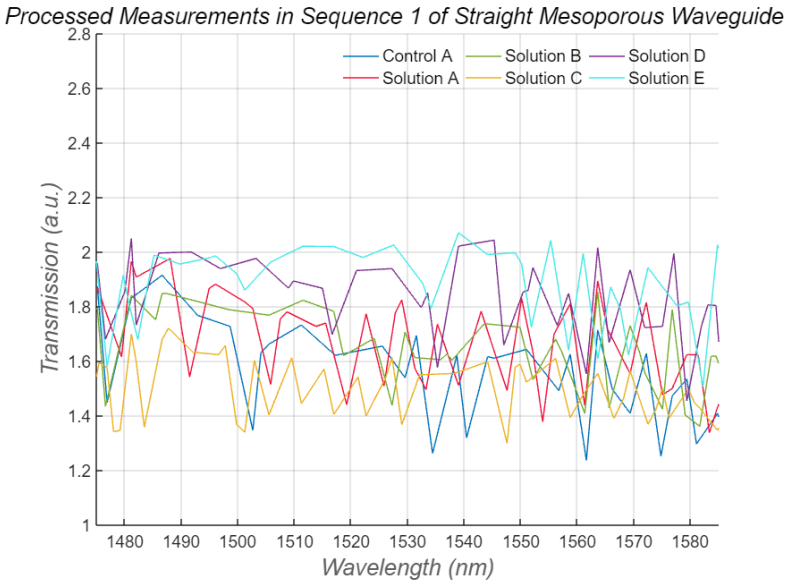

Figure 5.5: Plot of the maximum peaks of the measurements in Sequence 1 to visualize relation between the solutions. Control A in blue, Solution A in red, Solution B in green, Solution C in yellow, Solution D in purple, and Solution E in cyan. An overview of the solution compositions is found in table 4.4.

The dark blue graph showing control measurement A has the overall lowest transmission, showing that the waveguide has lower transmission without any solution present. Furthermore, the measurements with Solution D and E have the highest transmission, indicating that higher concentrations of ethanol (75% and 100%) give better transmission in the mesoporous waveguide, as expected and discussed above.

However, an irregularity observed in these graphs is the low transmission in Solution C with 50% ethanol and water. This might have been caused by several factors such as contamination in the solution, uncertain alignment of the chip and weak coupling between the fibers and waveguide. The most likely cause is sub-optimal coupling. As both aligning the chip on the stage and coupling in is done manually and repeated after every solution, there will be a difference in the chip position and coupling that can affect the transmission detected. Methods to avoid this and improve the laboratory setup are discussed later in the summarized discussion section.

Sequence 2 of measurements was performed with the same solutions as Sequence 1 to observe reproducability and patterns in the measurements, hence, the same results and takeaways are expected. Figure 5.6 shows the processed data from the measurements in Sequence 2 and figure 5.7 shows the plotted maxiumum peaks.

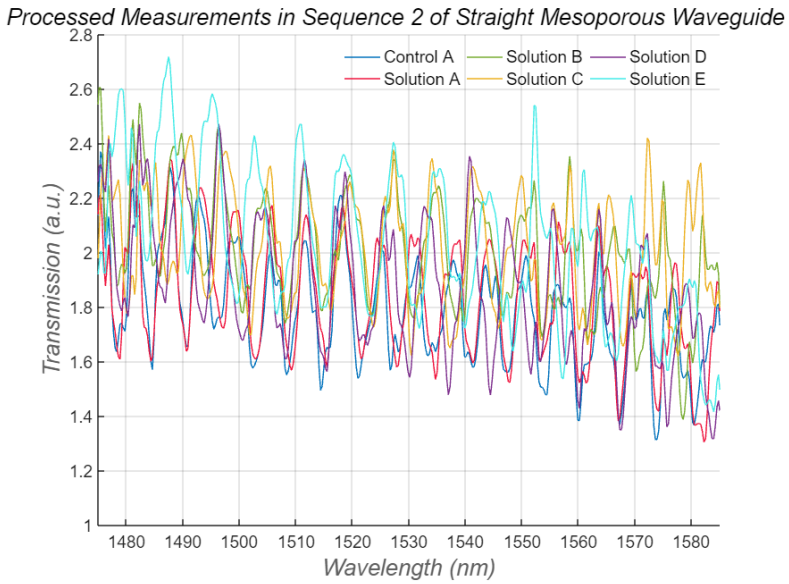

Figure 5.6: Processed measurements in Sequence 2; Control A in blue, Solution A in red, Solution B in green, Solution C in yellow, Solution D in purple, and Solution E in cyan. An overview of the solution compositions is found in table 4.4.

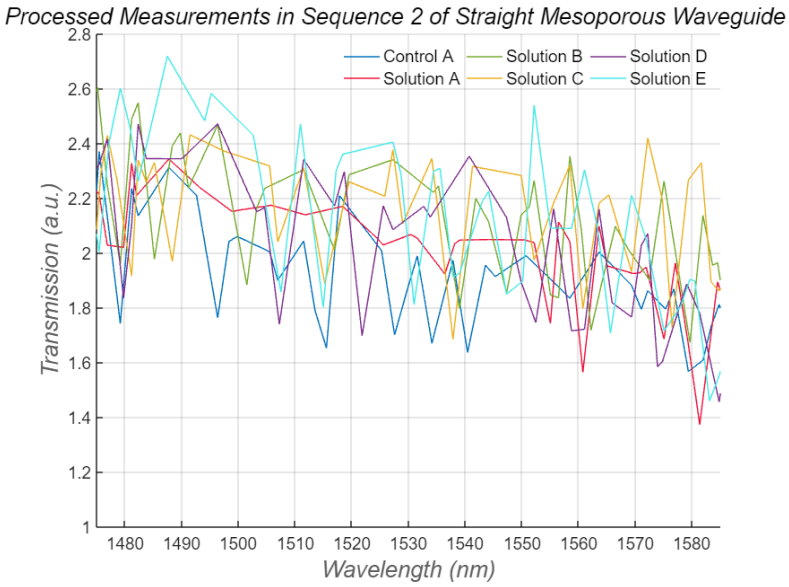

Figure 5.7: Plot of the maximum peaks of the measurements in Sequence 2 to visualize relation between the solutions. Control A in blue, Solution A in red, Solution B in green, Solution C in yellow, Solution D in purple, and Solution E in cyan. An overview of the solution compositions is found in table 4.4.

Observations in figure 5.7 are similar to observations in 5.5. The highest concentrations of ethanol (Solution C, D and E), have the highest transmission, while the control measurement and Solution A have the lowest transmission. Nevertheless, the overall transmission of all solutions is 0.2-0.6 units higher than in Sequence 1. Again, this can be explained by the coupling efficiency and alignment of the system as the second sequence was potentially better aligned.

In contrast to Sequence 1 and 2, measurements in *Sequence 3* were made using different concentrations of ethanol and methanol. The refractive index of methanol is lower than the refractive index of both ethanol and water at $n_{methanol} = 1.31$. Furthermore, the confinement factor in the mesoporous optical waveguide with the porosity of $p = 38\%$ when using methanol solution is 1% lower than when using ethanol and 1.69% lower than when using water. This indicates that the field is less confined in the waveguide penetrated with methanol than in the waveguide penetrated with ethanol and will therefore have lower transmission. The absorption coefficient spectra of ethanol, methanol and water outlined in section 3.3.3 give an indication of the expected results of Sequence 3 in comparison to Sequence 1 and 2. The spectra of ethanol and methanol have similar wide peaks around 1580nm, but methanol has a higher peak absorption coefficient of $\alpha_{methanol} = 1.1 \times 10^{-6}$ than ethanol; $\alpha_{ethnaol} = 6.9 \times 10^{-7}$. Furthermore, methanol overall has lower absorption than water in this range. This shows that solutions with methanol and ethanol overall have lower absorption than solutions with water and ethanol. The transmission with ethanol and methanol solutions should therefore overall be higher than with solutions of ethanol and water, but solutions with high ethanol content will have higher transmission than solutions with higher methanol content. This can also be confirmed from the transmission calculations in table 5.4 where the transmission in ethanol is higher than in methanol.

Figure 5.8 shows the results from measurement *Sequence 3* and figure 5.9 shows the plotted peaks. Control A was measured without any solution as before. Solution F contains 100% methanol, Solution G contains 25% ethanol and 75% methanol, Solution H contains 50% eth-

anol and 50% methanol and Solution I contains 75% ethanol and 25% methanol. In addition to the measurements in Sequence 3, the results from Solution E in Sequence 2 are also added to the figures below to compare and contrast the effects of 100% ethanol to the solutions of methanol and ethanol.

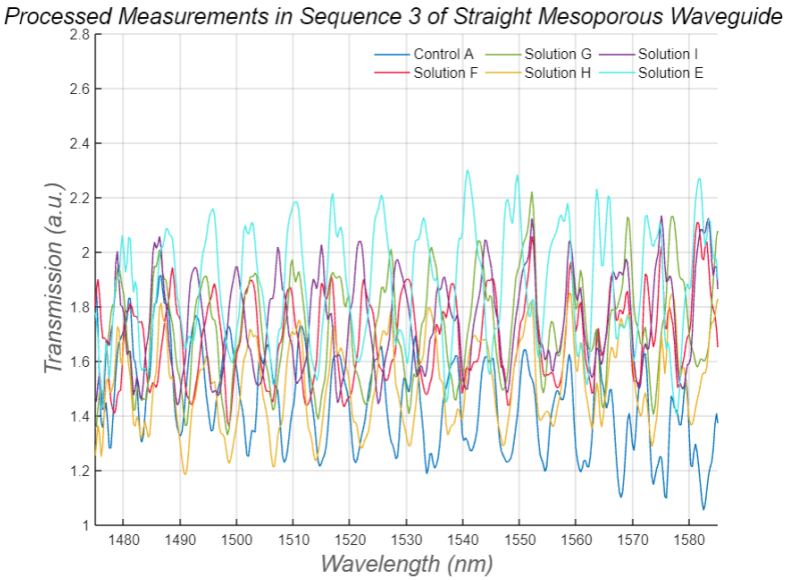

Figure 5.8: Processed measurements in Sequence 3; Control A in blue, Solution F in red, Solution G in green, Solution H in yellow, Solution I in purple, and Solution E in cyan. An overview of the solution compositions is found in table 4.4.

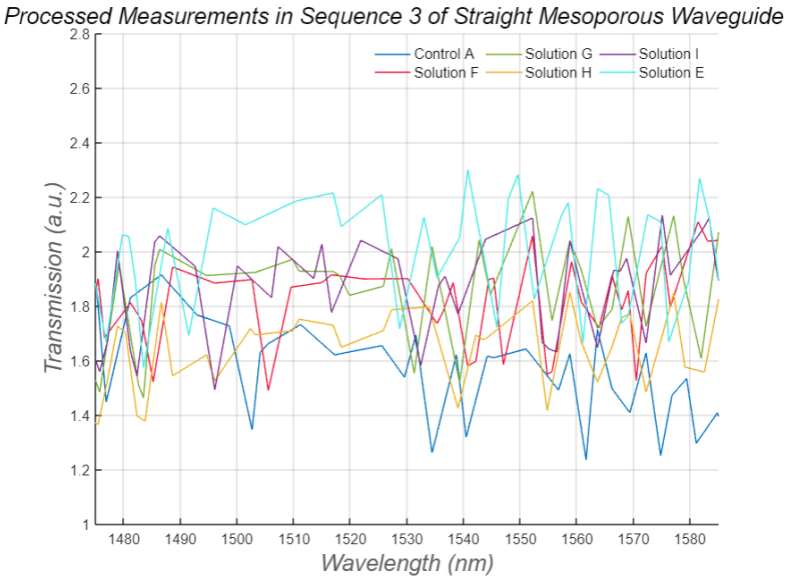

Figure 5.9: Plot of the maximum peaks of the measurements in Sequence 3 to visualize relation between the solutions. Control A in blue, Solution F in red, Solution G in green, Solution H in yellow, Solution I in purple, and Solution E in cyan. An overview of the solution compositions is found in table 4.4.

Once more, the outcome of the measurements with different ethanol concentrations show

that higher concentrations of ethanol (Solution G, I and E) give better transmission. However, Solution H is irregular and has lower transmission than the other solutions with lower concentrations of ethanol. Again, this may have been caused by human error while coupling. In comparison to measurements with water and ethanol, the maximum peaks of transmission in Sequence 3 are generally lower than Sequence 2 measurements, but slightly higher than Sequence 1. As the expected result was to have higher transmission in solutions with ethanol and methanol rather than ethanol and water, this is irregular. The reasons for the unexpected results may again be explained with the irregular coupling of the waveguide.

Generally, an uncertainty in all transmission measurements is not knowing the extent at which solutions penetrate the mesoporous core of the waveguide. This forces the assumption that all solutions penetrate the same. Also, even though the sample is heated between every new solution to allow for evaporation out of the pores, there cannot be certainty in that the pores are empty before the addition of new solution. This may affect the transmission in the next measurement set.

5.4 Summarized Discussion

Generally, the transmission in the mesoporous optical waveguide was best when using high concentrations of ethanol as top cladding. This reflects the theory about confinement factor and absorption in the solvents. The simulations further support that ethanol has lower absorption in the mesoporous waveguide. Improvements in the laboratory setup for the transmission measurements may reduce the uncertainties in measurements and allow for more efficient research. Firstly, incorporating a pump system ensuring a continuous flow of solution instead of removing the sample from the coupled position to change the solution could be implemented. This addition reduces, if not eliminates, the human error experienced due to the repetition of coupling and alignment. It would also reduce time needed to measure transmission with multiple solutions as coupling and adjusting alignment was tedious in the setup used for this thesis. However, the sample would have to be aligned on a hot plate to still be able to incorporate the evaporation of solution from the pores between the different measurement sets. This would also require that the lid or closing mechanism of the microfluidic cell was removable without disturbing the coupling of the waveguide to allow for evaporation. Secondly, fabricating a microfluidic cell where more of the waveguide on the chip may be covered by the dispensed solution could further improve the setup. This would allow for more light-matter interaction of the analyte and possibly reveal more sensitive results in transmission spectra. A pump system with a custom microfluidic cell has previously been utilized in other microfluidic research involving waveguides [22], but due to time constraints and uncertainty involving the size of the mesoporous waveguide chip it was not implemented for this thesis. However, incorporating a similar microfluidic cell structure and pump system is a possibility for future work. Another suggestion to future work is to experiment with the functionalization of the mesoporous waveguide core as performed in [22], specifically of the pores within the core. This could further attract solution into the pores and improve sensing abilities.

Chapter 6

Conclusion

The objectives of this thesis have been to investigate the possibilities for liquid sensing with mesoporous optical waveguides by examining the correlation between porosity and confinement factor, analysing the waveguide confinement with liquid solutions as top cladding and exploring the effect on transmission when using liquid as top cladding. The research was performed through simulations using Ansys Lumerical's MODE solver, fabrication of a PDMS microfluidic cell, and characterization using ellipsometry and transmission measurements with a tunable laser setup.

The results from simulations in this thesis prove that with air as the top cladding of a mesoporous optical waveguide, the confinement factor in the analyte is highest with porosities between $30\% \leq p \leq 35\%$, while with water as the top cladding, the confinement factor within the water in the pores and cladding, increases with increased porosity within the investigated range. This indicates that a highly porous core is preferable when using a mesoporous waveguide for liquid sensing. The simulations of confinement factor in the mesoporous waveguide with the characteristics of the fabricated waveguide, further reveal that the confinement within the cladding is generally higher for liquids than for air when using the same porosity. This points at more light-matter interaction in liquids than in gas on mesoporous waveguides, and shows that the electromagnetic field is leaking more into the substrate when using air as top cladding. These calculations, combined with analysis of the absorption spectra in the wavelength range of $1300nm \leq \lambda \leq 1700nm$, for the solutions water, ethanol and methanol, also revealed that the transmission in the waveguide when using ethanol as the top cladding should be two times higher than the transmission when using pure water as cladding. Moreover, with a top cladding of methanol, the transmission should be half of the transmission when using an ethanol top cladding in this wavelength range, concluding that of the tested solutions, the transmission in the mesoporous waveguide should be highest when using ethanol.

Characterization of the mesoporous optical waveguide with ellipsometry showed that the fabricated waveguide chip had a core thickness of $h = 439nm$, the refractive index of the TiO_2 core was $n = 1.89$ and the core porosity was $p = 38\%$. The transmission measurements were performed with solutions of ethanol and water of different concentration, and with solutions of ethanol and methanol of different concentration, as top cladding. Measurements were also performed without solution present as a control measurement. The measurements confirm the results from the simulations; the solutions tested with high concentrations of ethanol, gave the highest transmission spectra, while the measurements performed with pure water and pure methanol allowed for lower transmission in the waveguide. Some uncertainties were observed and were concluded to be caused by irregularities during coupling of the waveguide.

Improvements to the laboratory setup were suggested and are included below in suggestions for future work.

Overall, the investigations made into the possibilities for liquid sensing using mesoporous optical waveguides conclude that the design is promising. The confinement factors of the analyzed solutions are high, indicating high light-matter interaction, and the waveguide transmission experiences expected changes related to the solutions disposed as top cladding. Of the solutions tested, the one with the lowest absorption in the experimental range, ethanol, experienced the highest transmission, as expected from theory and simulations. The experimental setup and procedures proved favourable for the thesis objectives. The findings presented in this thesis give solid basis for future research on the use of mesoporous optical waveguides for liquid sensing in for instance biomedical applications.

6.1 Future Work

To continue research on the use of mesoporous optical waveguides for liquid sensing, some adjustments to the laboratory setup and procedure should be considered. Specifically, using a pump system in the setup and investigating the effect of preconcentration of solutions and functionalization of the pores.

Suggestions for improvements in the laboratory setup are, as discussed, to include a pump system to interchange the solutions used as top cladding, and ultimately limit the errors caused by irregular coupling of the waveguide by keeping the sample in the same position throughout the measurements. This would demand a redesign of the microfluidic cell to include access to tubes for the pump.

Research into the effects of preconcentrating solutions before testing them on the mesoporous waveguide, as well as techniques for functionalization of the pores within the core, exhibits potential for future work. These improvements could lead to improved sensing abilities of a sensor based on the principle of a mesoporous waveguide core for liquid sensing.

Moreover, to further explore the capabilities of the mesoporous optical waveguide as a liquid sensor, different solutions with different absorption spectra should be tested.

Bibliography

[1] M. Vlk, A. Datta, S. Alberti, H. D. Yallew, V. Mittal, G. S. Murugan and J. Jágerská, 'Extraordinary evanescent field confinement waveguide sensor for mid-infrared trace gas spectroscopy,' *Light: Science & Applications*, vol. 10, no. 1, p. 26, Jan. 2021, ISSN: 2047-7538. DOI: 10.1038/s41377-021-00470-4. [Online]. Available: https://doi.org/10.1038/s41377-021-00470-4.

[2] C. A. Barrios, 'Optical slot-waveguide based biochemical sensors,' *Sensors*, vol. 9, no. 6, pp. 4751–4765, 2009, ISSN: 1424-8220. DOI: 10.3390/s90604751. [Online]. Available: https://www.mdpi.com/1424-8220/9/6/4751.

[3] B. E. A. Saleh and M. C. Teich, *Fundamentals of Photonics, Third Edition, Chapter 5: Electromagnetic Optics*. John Wiley & Sons, Inc., 2019.

[4] B. E. A. Saleh and M. C. Teich, *Fundamentals of Photonics, Third Edition, Chapter 6: Guided-Wave Optics*. John Wiley & Sons, Inc., 2019.

[5] B. E. A. Saleh and M. C. Teich, *Fundamentals of Photonics, Third Edition, Chapter 9: Guided-Wave Optics*. John Wiley & Sons, Inc., 2019.

[6] D. F. Swinehart, 'The beer-lambert law,' *Journal of Chemical Education*, vol. 39, no. 7, p. 333, 1st Jul. 1962, Publisher: American Chemical Society, ISSN: 0021-9584. DOI: 10.1021/ed039p333. [Online]. Available: https://doi.org/10.1021/ed039p333.

[7] M. Vlk, 'Optical waveguides for infrared spectroscopic detection of molecular gases,' Ph.D. dissertation, The Arctic University of Norway, 2021.

[8] 'Theory of integrated optic waveguides,' in *Integrated Photonics: Fundamentals*. John Wiley & Sons, Ltd, 2003, ch. 3, pp. 52–97, ISBN: 9780470861400. DOI: https://doi.org/10.1002/0470861401.ch3. eprint: https://onlinelibrary.wiley.com/doi/pdf/10.1002/0470861401.ch3. [Online]. Available: https://onlinelibrary.wiley.com/doi/abs/10.1002/0470861401.ch3.

[9] T. Visser, H. Blok, B. Demeulenaere and D. Lenstra, 'Confinement factors and gain in optical amplifiers,' *IEEE Journal of Quantum Electronics*, vol. 33, no. 10, pp. 1763–1766, 1997. DOI: 10.1109/3.631280.

[10] F. Dullo, J.-C. Tinguely, S. Solbø and O. Helleso, 'Single-mode limit and bending losses for shallow rib si3n4 waveguides,' *IEEE Photonics Journal*, vol. 7, pp. 1–1, Feb. 2015. DOI: 10.1109/JPHOT.2014.2387252.

[11] A. Lumerical. 'Solving bent waveguides in fde and feem.' (), [Online]. Available: https://optics.ansys.com/hc/en-us/articles/360034917253-Solving-bent-waveguides-in-FDE-and-FEEM (visited on 02/01/2023).

[12] S. Hong, L. Zhang, Y. Wang, M. Zhang, Y. Xie and D. Dai, 'Ultralow-loss compact silicon photonic waveguide spirals and delay lines,' *Photon. Res.*, vol. 10, no. 1, pp. 1–7, Jan. 2022. DOI: 10.1364/PRJ.437726. [Online]. Available: https://opg.optica.org/prj/abstract.cfm?URI=prj-10-1-1.

[13] D. Schwarz, H. Wormeester and B. Poelsema, 'Validity of Lorentz–Lorenz equation in porosimetry studies,' *Thin Solid Films*, vol. 519, no. 9, pp. 2994–2997, 2011, ISSN: 0040-6090. DOI: https://doi.org/10.1016/j.tsf.2010.12.053. [Online]. Available: https://www.sciencedirect.com/science/article/pii/S0040609010016834.

[14] D. A. G. Bruggeman, 'Berechnung verschiedener physikalischer konstanten von heterogenen substanzen. i. dielektrizitätskonstanten und leitfähigkeiten der mischkörper aus isotropen substanzen,' *Annalen der Physik*, vol. 416, no. 7, pp. 636–664, 1935. DOI: https://doi.org/10.1002/andp.19354160705. eprint: https://onlinelibrary.wiley.com/doi/pdf/10.1002/andp.19354160705. [Online]. Available: https://onlinelibrary.wiley.com/doi/abs/10.1002/andp.19354160705.

[15] M. Born, E. Wolf, A. B. Bhatia, P. C. Clemmow, D. Gabor, A. R. Stokes, A. M. Taylor, P. A. Wayman and W. L. Wilcock, *Principles of Optics: Electromagnetic Theory of Propagation, Interference and Diffraction of Light*, 7th ed. Cambridge University Press, 1999. DOI: 10.1017/CBO9781139644181.

[16] A. Lumerical. 'Mode - finite difference eigenmode (fde) solver introduction.' (), [Online]. Available: https://optics.ansys.com/hc/en-us/articles/360034917233-MODE-Finite-Difference-Eigenmode-FDE-solver-introduction (visited on 16/06/2022).

[17] A. Lumerical. 'Mode product reference manual.' (), [Online]. Available: https://optics.ansys.com/hc/en-us/articles/360020687354 (visited on 09/12/2022).

[18] Z. Zhu and T. G. Brown, 'Full-vectorial finite-difference analysis of microstructured optical fibers,' *Opt. Express*, vol. 10, no. 17, pp. 853–864, Aug. 2002. DOI: 10.1364/OE.10.000853. [Online]. Available: https://opg.optica.org/oe/abstract.cfm?URI=oe-10-17-853.

[19] K. Yee, 'Numerical solution of initial boundary value problems involving maxwell's equations in isotropic media,' *IEEE Transactions on Antennas and Propagation*, vol. 14, no. 3, pp. 302–307, 1966. DOI: 10.1109/TAP.1966.1138693.

[20] S. Alberti and J. Jágerská, 'Sol-gel thin film processing for integrated waveguide sensors,' *Frontiers in Materials*, vol. 8, 2021, ISSN: 2296-8016. DOI: 10.3389/fmats.2021.629822. [Online]. Available: https://www.frontiersin.org/articles/10.3389/fmats.2021.629822.

[21] A. Mahmood and A. Naeem, 'Sol-gel-derived doped zno thin films: Processing, properties, and applications,' in *Recent Applications in Sol-Gel Synthesis*, U. Chandra, Ed., Rijeka: IntechOpen, 2017, ch. 9. DOI: 10.5772/67857. [Online]. Available: https://doi.org/10.5772/67857.

[22] J. Høvik, M. Yadav, N. B. Arnfinnsdottir and A. Aksnes, 'Lab-on-a-chip photonic biosensor for detection of antigens,' in *Biosensing and Nanomedicine XI*, H. Mohseni, M. H. Agahi and M. Razeghi, Eds., International Society for Optics and Photonics, vol. 10728, SPIE, 2018, p. 1 072 806. DOI: 10.1117/12.2321128. [Online]. Available: https://doi.org/10.1117/12.2321128.

[23] C.-W. Tsao, 'Polymer microfluidics: Simple, low-cost fabrication process bridging academic lab research to commercialized production,' *Micromachines*, vol. 7, no. 12, p. 225, Dec. 2016, ISSN: 2072-666X. DOI: 10.3390/mi7120225. [Online]. Available: http://dx.doi.org/10.3390/mi7120225.

[24] J. Theeten and D. Aspnes, 'Ellipsometry in thin film analysis,' *Annual Review of Materials Science*, vol. 11, no. 1, pp. 97–122, 1981.

[25] V.-M. Airaksinen, 'Chapter 15 - silicon wafer and thin film measurements,' in *Handbook of Silicon Based MEMS Materials and Technologies (Second Edition)*, ser. Micro and Nano Technologies, M. Tilli, T. Motooka, V.-M. Airaksinen, S. Franssila, M. Paulasto-Kröckel and V. Lindroos, Eds., Second Edition, Boston: William Andrew Publishing, 2015, pp. 381–390, ISBN: 978-0-323-29965-7. DOI: https://doi.org/10.1016/B978-0-323-29965-7.00015-4. [Online]. Available: https://www.sciencedirect.com/science/article/pii/B9780323299657000154.

[26] M. Schubert, '9 - Theory and Application of Generalized Ellipsometry,' in *Handbook of Ellipsometry*, H. G. Tompkins and E. A. Irene, Eds., Norwich, NY: William Andrew Publishing, 2005, pp. 637–717, ISBN: 978-0-8155-1499-2. DOI: https://doi.org/10.1016/B978-081551499-2.50011-3. [Online]. Available: https://www.sciencedirect.com/science/article/pii/B9780815514992500113.

[27] 'Spectral analysis,' in *Infrared Spectroscopy: Fundamentals and Applications*. John Wiley & Sons, Ltd, 2004, ch. 3, pp. 45–70, ISBN: 9780470011140. DOI: https://doi.org/10.1002/0470011149.ch3. eprint: https://onlinelibrary.wiley.com/doi/pdf/10.1002/0470011149.ch3. [Online]. Available: https://onlinelibrary.wiley.com/doi/abs/10.1002/0470011149.ch3.

[28] A. Savitzky and M. J. E. Golay, 'Smoothing and differentiation of data by simplified least squares procedures.,' *Analytical Chemistry*, vol. 36, no. 8, pp. 1627–1639, 1964. DOI: 10.1021/ac60214a047. eprint: https://doi.org/10.1021/ac60214a047. [Online]. Available: https://doi.org/10.1021/ac60214a047.

[29] Q. Kong, T. Siauw and A. M. Bayen, 'Chapter 17 - interpolation,' in *Python Programming and Numerical Methods*, Q. Kong, T. Siauw and A. M. Bayen, Eds., Academic Press, 2021, pp. 295–313, ISBN: 978-0-12-819549-9. DOI: https://doi.org/10.1016/B978-0-12-819549-9.00027-0. [Online]. Available: https://www.sciencedirect.com/science/article/pii/B9780128195499000270.

[30] G. M. Hale and M. R. Querry, 'Optical constants of water in the 200-nm to 200-μm wavelength region,' *Appl. Opt.*, vol. 12, no. 3, pp. 555–563, Mar. 1973. DOI: 10.1364/AO.12.000555. [Online]. Available: https://opg.optica.org/ao/abstract.cfm?URI=ao-12-3-555.

[31] T. L. Myers, R. G. Tonkyn, T. O. Danby, M. S. Taubman, B. E. Bernacki, J. C. Birnbaum, S. W. Sharpe and T. J. Johnson, 'Accurate measurement of the optical constants n and k for a series of 57 inorganic and organic liquids for optical modeling and detection,' *Applied Spectroscopy*, vol. 72, no. 4, pp. 535–550, 2018, PMID: 29286824. DOI: 10.1177/0003702817742848. eprint: https://doi.org/10.1177/0003702817742848. [Online]. Available: https://doi.org/10.1177/0003702817742848.

[32] D. T. Pierce and W. E. Spicer, 'Electronic structure of amorphous si from photoemission and optical studies,' *Phys. Rev. B*, vol. 5, pp. 3017–3029, 8 Apr. 1972. DOI: 10.1103/PhysRevB.5.3017. [Online]. Available: https://link.aps.org/doi/10.1103/PhysRevB.5.3017.

[33] L. Gao, F. Lemarchand and M. Lequime, 'Exploitation of multiple incidences spectrometric measurements for thin film reverse engineering,' *Opt. Express*, vol. 20, no. 14, pp. 15 734–15 751, Jul. 2012. DOI: 10.1364/OE.20.015734. [Online]. Available: https://opg.optica.org/oe/abstract.cfm?URI=oe-20-14-15734.

[34] J. Rantala and A. Kärkkäinen, 'Optical properties of spin-on deposited low temperature titanium oxide thin films,' *Optics express*, vol. 11, pp. 1406–10, Jul. 2003. DOI: 10.1364/OE.11.001406.

[35] 'Thorlabs - TLK-l1550m tunable laser kit, 1550 nm, littman configuration, FC/APC.' (), [Online]. Available: https://www.thorlabs.us (visited on 27/06/2023).

[36] S. Alberti, A. Datta and J. Jágerská, 'Integrated nanophotonic waveguide-based devices for ir and raman gas spectroscopy,' *Sensors (Basel)*, vol. 21, no. 21, p. 7224, Oct. 2021, ISSN: 1424-8220. DOI: 10.3390/s21217224. [Online]. Available: https://doi.org/10.3390/s21217224.

[37] *Semilab | Products*. [Online]. Available: https://semilab.com/category/products/spectroscopic-ellipsometry-5 (visited on 05/01/2023).

[38] T. Easwarakhanthan, D. Beyssen, L. Le Brizoual and P. Alnot, 'Forouhi-bloomer and tauc-lorentz optical dispersions applied using spectroscopic ellipsometry to plasma-deposited fluorocarbon films,' *Journal of Applied Physics*, vol. 101, no. 7, p. 073 102, 2007. DOI: 10.1063/1.2719271. eprint: https://doi.org/10.1063/1.2719271. [Online]. Available: https://doi.org/10.1063/1.2719271.

[39] N. Liu, J. Zhang, Z. Zhu, W. Xu and K. Liu, 'Efficient coupling between an integrated photonic waveguide and an optical fiber,' *Opt. Express*, vol. 29, no. 17, pp. 27 396–27 403, Aug. 2021, Publisher: Optica Publishing Group. DOI: 10.1364/OE.430644. [Online]. Available: https://opg.optica.org/oe/abstract.cfm?URI=oe-29-17-27396.

[40] 'Product.' (), [Online]. Available: https://www.ni.com/en-no/shop/software/products/labview.html (visited on 28/06/2023).

Appendix A

Script for confinement factor calculation in Ansys Lumerical

Retrieved and improved for specific use from [7].

```
##################################################################
# This script finds parameters of the fundamental mode of
# a rib waveguide. Both for its core and cladding.
#================================================================


#================================================================
# Calculating for core of waveguide
#================================================================
# Enter refractive index value of the core medium:
index_val = 1.89;
mode = "mode1"; # select your mode
porosity = 0.38;

# Creating a binary mask to define c.f. region:
# Get the actual index data:
index_x = real(pinch(getdata("FDE::data::material","index_x")));
# Retrieve the matrix size:
x = pinch(getdata("FDE::data::material","x"));
nx = length(x);
y = pinch(getdata("FDE::data::material","y"));
ny = length(y);
filter = matrix(nx,ny); # define the mask matrix
# Define the mask; put values into mask matrices:
rel_dif = 0.01; # something like an error for the ref. index
index_val_mat = ones(nx,ny)*index_val;
filter(1:nx,1:ny) = almostequal(pinch(index_x), index_val_mat, rel_dif);
clear(index_x, nx, ny, rel_dif, index_val_mat); # clear unnecessary data
# Retrieve the field data of a given mode:
Ex = pinch(getdata("FDE::data::"+mode,"Ex"));
Ey = pinch(getdata("FDE::data::"+mode,"Ey"));
```

```
Ez = pinch(getdata("FDE::data::"+mode,"Ez"));
Hx = pinch(getdata("FDE::data::"+mode,"Hx"));
Hy = pinch(getdata("FDE::data::"+mode,"Hy"));
# Calculate Pz and |E| squared:
Py = (Ex*conj(Hy) - Ez*conj(Hx));
# factor 0.5 is important due to fields described with complex numbers
Enorm2 = Ex*conj(Ex) + Ey*conj(Ey) + Ez*conj(Ez);

# Apply a mask to |E| squared:
Enorm2_f = Enorm2*filter; # filtered

# Confinement factor calculation and acquisition:
intP = integrate(real(Py), [1,2], x, y);
intE_f = integrate(real(Enorm2_f), [1,2], x, y);
CF_core = c * eps0 * index_val * intE_f / intP;
clear(index_val, x, y, Ex, Ey, Ez, Hx, Hy, Py, Enorm2, Enorm2_f, intP,
↪  intE_f); # clear unnecessary data
?mode + " confinement factor of core is " + num2str(abs(CF_core)*100) + "%";

#=============================================================
# Calculating for cladding of waveguide
#=============================================================
# Enter refractive index value of the cladding medium:
index_val = 1.35;
mode = "mode1"; # select your mode

# Creating a binary mask to define c.f. region:
# Get the actual index data:
index_x = real(pinch(getdata("FDE::data::material","index_x")));
# Retrieve the matrix size:
x = pinch(getdata("FDE::data::material","x"));
nx = length(x);
y = pinch(getdata("FDE::data::material","y"));
ny = length(y);
filter = matrix(nx,ny); # define the mask matrix
# Define the mask; put values into mask matrices:
rel_dif = 0.01; # something like an error for the ref. index
index_val_mat = ones(nx,ny)*index_val;
filter(1:nx,1:ny) = almostequal(pinch(index_x), index_val_mat, rel_dif);
clear(index_x, nx, ny, rel_dif, index_val_mat); # clear unnecessary data
# Retrieve the field data of a given mode:
Ex = pinch(getdata("FDE::data::"+mode,"Ex"));
Ey = pinch(getdata("FDE::data::"+mode,"Ey"));
Ez = pinch(getdata("FDE::data::"+mode,"Ez"));
Hx = pinch(getdata("FDE::data::"+mode,"Hx"));
Hy = pinch(getdata("FDE::data::"+mode,"Hy"));
# Calculate Pz and |E| squared:
Py = (Ex*conj(Hy) - Ez*conj(Hx));
```

```
# factor 0.5 is important due to fields described with complex numbers
Enorm2 = Ex*conj(Ex) + Ey*conj(Ey) + Ez*conj(Ez);

# Apply a mask to |E| squared:
Enorm2_f = Enorm2*filter; # filtered

# Confinement factor calculation and acquisition:
intP = integrate(real(Py), [1,2], x, y);
intE_f = integrate(real(Enorm2_f), [1,2], x, y);
CF_cladding = c * eps0 * index_val * intE_f / intP;
clear(index_val, x, y, Ex, Ey, Ez, Hx, Hy, Py, Enorm2, Enorm2_f, intP,
 ↪  intE_f); # clear unnecessary data
?mode + " confinement factor of cladding is " + num2str(abs(CF_cladding)*100)
 ↪  + "%";

##################################################################

?mode + " confinement factor in pores is " +
 ↪  num2str(((abs(CF_core)*porosity)+(abs(CF_cladding)))*100) + "%";
```

Appendix B

Mask for Lithography Fabrication

Previously designed by Jana Jágerská and Sebastián Alberti.

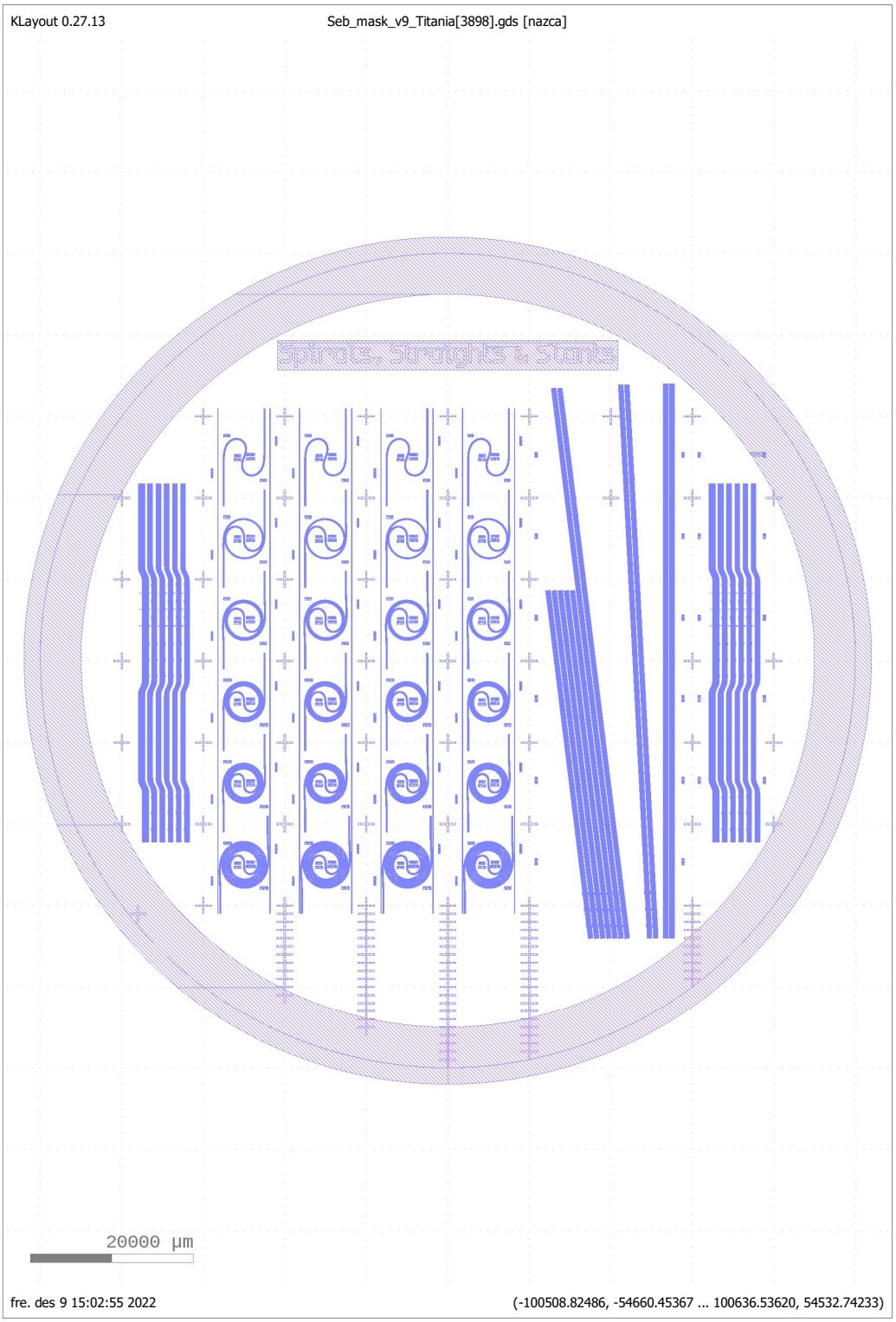
KLayout 0.27.13
Seb_mask_v9_Titania[3898].gds [nazca]
Spirals, Straights & Stubs
20000 µm
fre. des 9 15:02:55 2022
(-100508.82486, -54660.45367 ... 100636.53620, 54532.74233)

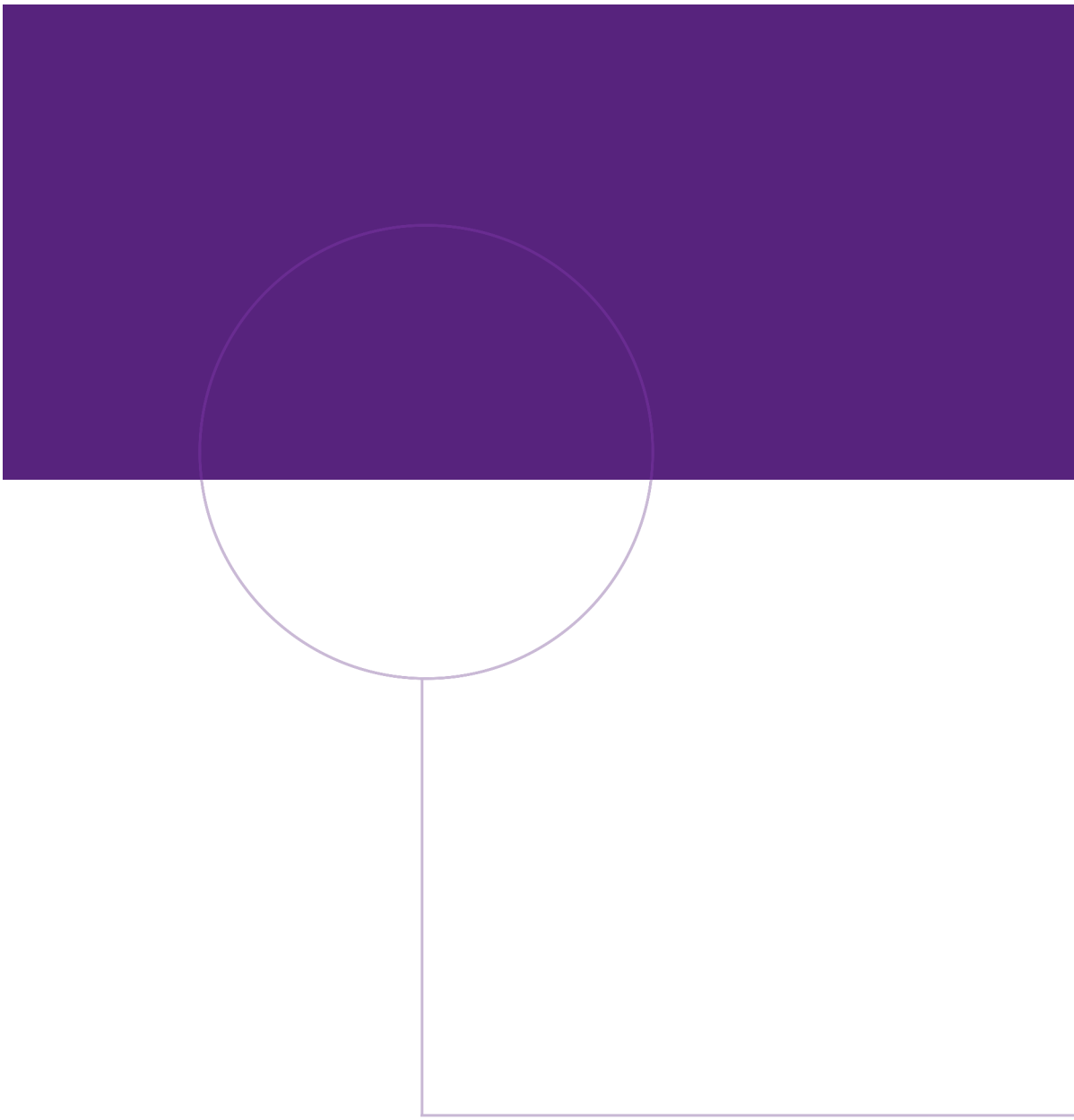

NTNU

Norwegian University of
Science and Technology